

Contents lists available at ScienceDirect

# Progress in Energy and Combustion Science

journal homepage: www.elsevier.com/locate/pecs



# Mesoscale modeling in electrochemical devices—A critical perspective



Emily M. Ryan<sup>a,\*</sup>, Partha P. Mukherjee<sup>b,\*</sup>

- <sup>a</sup> Department of Mechanical Engineering, Boston University, 110 Cummington Mall, 02215 Boston, MA, United States
- <sup>b</sup> School of Mechanical Engineering, Purdue University, West Lafayette, IN, United States

#### ARTICLE INFO

#### Article history: Received 8 June 2018 Accepted 27 November 2018

Keywords:
Electrochemical energy systems
Mesoscale modeling
Porous electrode
Microstructure
Property
Performance

#### ABSTRACT

Electrochemical energy systems, such as batteries and fuel cells, are being developed for applications ranging from portable devices and electric vehicles to large-scale grid storage. These advanced energy conversion and storage technologies will be a critical aspect of a sustainable energy future and promise to provide cleaner, more efficient energy. Computational modeling at various scales from nanoscale ab initio modeling to macroscale system and controls level modeling, has been a central part of the electrochemical energy research. Much of the complex interactions due to the electrochemistry coupled transport phenomena occur at the interfaces and within the porous electrode microstructures. This is often referred to as the mesoscale and plays a critical role in the operation and efficiency of electrochemical devices. In this critical perspective, we discuss the state-of-the-art, challenges and path forward in mesoscale modeling of electrochemical energy systems and their application to various design and operational issues in solid oxide fuel cells, polymer electrolyte membrane fuel cells, lithium ion batteries and metal-air batteries. Particular focus is given to particle-based methods and fine-scale computational fluid dynamics based direct numerical simulation techniques, along with the challenges and advantages of these methods. Notable results from mesoscale modeling are presented along with discussions of the advantages, disadvantages and challenges facing mesoscale model development. This in-depth perspective is envisioned to serve as a primer to the critical role mesoscale modeling is poised to play in advancing the science and engineering of electrochemical energy systems.

© 2018 Elsevier Ltd. All rights reserved.

# **Contents**

		Introduction				
2.	Electi	rochemical physics	119			
	2.1.	Electrochemistry and chemical reactions	120			
		Charge transport				
		Advection-diffusion-migration				
	2.4.	2.4. Heat transfer 12				
	2.5.	Distinction between direct numerical simulation and macrohomogeneous model	123			
3.	Mesoscale modeling methods					
	3.1.	Porous microstructure representation				
		3.1.1. Experimental imaging				
		3.1.2. Stochastic reconstruction	125			
	3.2.	Particle methods	127			

Acronyms: BGK, Bhatnagar–Gross–Krook; CFD, computational fluid dynamics; CL, catalyst layer; DEM, discrete element method; DNS, direct numerical simulation; DPD, dissipative particle dynamics; FEM, finite element method; FIB-SEM, focused ion beam – scanning electron microscopy; FVM, finite volume method; GDL, gas diffusion layer; LBM, lattice Boltzmann method; LIB, lithium ion battery; MD, molecular dynamics; MPL, microporous layer; ORR, oxygen reduction reaction; PEFC, polymer electrolyte fuel cell; RVE, representative volume element; SOFC, solid oxide fuel cell; SPH, smoothed particle hydrodynamics; XCT, X-ray computed microtomography.

E-mail addresses: ryanem@bu.edu (E.M. Ryan), pmukherjee@purdue.edu (P.P. Mukherjee).

<sup>\*</sup> Corresponding authors.

		3.2.1.	Smoothed particle hydrodynamics fundamentals	128					
	3.2.2.	Dissi	pative particle dynamics fundamentals	128					
		3.2.3.	Lattice Boltzmann method fundamentals						
		3.2.4.	Notable results	129					
		3.2.5.	The far and a second and a second and a second a						
		3.2.6.	Challenges	132					
	3.3.	Fine-so	cale CFD	132					
		3.3.1.	DNS fundamentals: effective property estimation	133					
		3.3.2.	Notable results	134					
			Advantages and disadvantages						
		3.3.4.	Challenges	138					
4.	Summary								
5.	5. Challenges and future perspective								
	cknowledgements 13								
Refe	erences	5		140					

## 1. Introduction

The development of advanced electrochemical energy storage and conversion devices is critical to the development of a sustainable energy future. Electrochemical devices provide cleaner, more efficient energy than traditional fossil fuel burning systems and have the potential to significantly change the energy profile of the United States and the world. With the increasing use of intermittent, renewable energy sources, such as wind and solar, reliable energy storage is needed. Additionally, more efficient, longer lasting electrochemical devices are needed to increase the acceptance of alternative fuel vehicles, such as plugin hybrid, fuel cell, and battery electric vehicles.

Electrochemical storage and conversion devices cover a wide array of technologies such as batteries, fuel cells and capacitors. These technologies all operate along common physical principles but have distinct differences in their underlying multi-physical interactions and operational window. For example, solid oxide fuel cells (SOFCs) operate at high temperatures (600–1000 °C) and involve the transport of gaseous species through porous ceramic-based media; while, polymer electrolyte membrane fuel cells (PE-FCs) operate at lower temperatures (<100 °C) and involve multi-phase transport through multiple materials and layers.

Research into electrochemical devices has been ongoing for almost a century and has resulted in significant advances in technology. This research has involved a combination of both experimental and computational studies of the design, operation, safety, and performance of electrochemical devices. The complex microstructures and multi-physics of electrochemical devices require research to consider these devices at multiple scales and with a variety of experimental and computational tools. Computational modeling is particularly well suited for studying these systems given its ability to resolve the detailed physics occurring within them during operation, which cannot be observed experimentally.

Much of the critical physics of electrochemical devices occurs within the porous media of the device and at the interfaces between the electrodes and electrolyte. The physics occurring in these regions are considered mesoscale phenomena and typically take place on the micron to millimeter length scale. Mesoscale is the length and time scales between the nano-scale reactions and transport happening on the surfaces of materials and the macroscale operation of the electrochemical devices. The majority of the chemical and electrochemical reactions, temperature variations and stresses in electrochemical devices occur in the regions around the electrode-electrolyte interfaces of the cell and degradation of the electrochemical performance and structural stability often occurs in these regions. This makes understanding the mesoscale phenomena critical to the design of advanced electrochemical devices.

Computational studies of multiphase systems often occur at the two extremes of the system. Namely, the atomic level first principles scale or large-scale device modeling. While understanding the system at both of these scales is critical, it is not sufficient for understanding the physics or for designing new systems. While atomic level modeling can elucidate the reactions and surface interactions of the system, it cannot be scaled up to a level where the transport near the interface or in complicated multiphase geometries is resolved. At the other end, large-scale simulations are often used to study the overall performance of an electrochemical device, such as a battery, where the porous materials within the device are considered using a macrohomogeneous modeling approach, which homogenizes the porous media and characterizes it via bulk effective parameters without explicitly resolving the interfacial physics. In heterogeneous reactive systems, it has been shown that the accurate modeling of the transport through the structure is critical to accurately predicting the overall performance, this is especially critical in electrochemical devices. To accomplish this mesoscale modeling is needed that can accurately resolve the microstructure and the reactive transport within it.

In this article, we will review mesoscale computational modeling of electrochemical devices. The review will discuss the multiphysics phenomena at the mesoscale along with computational modeling methods used to consider electrochemical devices. The application of mesoscale modeling to various electrochemical devices will also be presented and will focus on fuel cell (SOFCs and PEFCs) and battery (lithium-ion, lithium-air) technologies. Specific examples of the use of mesoscale computational models to investigate the performance, stability and design of fuel cells and batteries will be presented along with a discussion of challenges and future perspectives for mesoscale modeling of electrochemical systems

# 2. Electrochemical physics

Electrochemical devices are inherently multiphysics systems, their performance is driven by the numerous physical phenomena occurring within them and the interactions and coupling between the different physics. These phenomena include the transport of charge and species, chemical and electrochemical reactions, and heat transfer. Mesoscale computational models need to accurately include these physics in their models to predict the performance and operation of the device. Additionally, mesoscale models that resolve the pore-scale phenomena can be used to formulate effective property models which are used in macrohomogeneous modeling methods. In the following sub-sections, the mesoscale governing equations for the multiphysics of electrochemical devices are discussed. It should be noted that the length scales considered to be mesoscale in this article are large enough that the continuum

governing equations are valid, as such the equations discussed in the following sub-sections are often very similar to the governing equations used in macroscale modeling.

#### 2.1. Electrochemistry and chemical reactions

Electrochemical reactions are the heart of an electrochemical device's operation. Depending on the system of interest the electrochemical reactions can take a variety of forms. In general, an oxidation reaction will occur in one electrode releasing electrons and a reduction reaction will occur in the other electrode consuming the electrons. For high temperature SOFCs the typical global electrochemical reaction for the anode and cathode can be written as an oxidation reaction of  $H_2$  with oxygen ions  $(O^{2-})$  in the anode,

$$H_2(f) + O^{2-}(e) \leftrightarrow H_2O(f) + 2e^{-}(s)$$
 (1)

where subscript f denotes species in the fluid phase, s in the electrode phase and e in the electrolyte phase, and a reduction reaction of  $O_2$  with electrons ( $e^-$ ) in the cathode,

$$\frac{1}{2}O_2(f) + 2e^-(s) \leftrightarrow O^{2-}(e) \tag{2}$$

The chemical reactions can be modeled as a source term (S) added to the advection-diffusion equation (Eq. (3))

$$\frac{\partial c_i}{\partial t} + \nabla \cdot (\vec{u}c_i) = \nabla \cdot J_i + \sum_{i=1}^{R} S_j$$
(3)

where c is the concentration,  $\vec{u}$  is the velocity vector, J is the diffusive flux, and S is summed over all reactions (R) involving species i. Treatment of electrochemical reactions occurring at the electrode-electrolyte interface can be done in two ways. For a homogenized representation of the electrode-electrolyte assembly, the interfacial electrochemical reactions can be modeled as the source term (S) while for the fine scale modeling on the completely resolved electrode microstructure, the interfacial reactions occur as interface conditions and boundary conditions for the governing differential equation. The aforementioned distinction is detailed in Section 2.5 using the intercalation-based lithium-ion battery (LIB) system as an example with appropriate governing differential equations and boundary/interface conditions.

In general, the reaction rates are mathematically related to species concentrations via the law of mass action, as shown in Eq. (4). Here, a distinction should be made that chemical reactions are typically homogeneous reaction, i.e., reactants and species are in the same phase and thus these are volumetric (bulk) reactions. On the other hand, the electrochemical reactions are, by their very nature, heterogeneous reactions and take place at an electrified interface. Atomistically speaking, electrochemical reactions are essentially made up of two distinct finite rate processes: (i) adsorption of bulk species at the interface, and (ii) subsequent reaction of adsorbed species. Depending on the chemical species involved, both reactants as well as products could be the adsorbed species. Generally, it is assumed that the adsorption of bulk species is a much faster process as compared to the electrochemical reaction step and in-turn the concentrations appearing in an electrochemical rate equation such as Eq. (4) are bulk concentrations while the reaction rate itself is an interfacial reaction rate (expressed in the units of mol/m<sup>2</sup>s). Generally, the species concentration exponents are stoichiometric coefficients in the balanced reaction. However, if the balanced reaction is composed of multiple simpler steps, then, effective coefficients would differ from the stoichiometric coefficients in the overall balance equation [1].

$$S_{i} = k_{fi} \prod_{i=1}^{s} c_{j}^{m_{fij}} - k_{ri} \prod_{i=1}^{s} c_{j}^{m_{rij}}$$

$$\tag{4}$$

where  $k_{fi}$  and  $k_{ri}$  are the forward and reverse reaction rate coefficients of reaction i and  $m_{ij}$  is the order of reaction i with re-

spect to species *j*. The reaction rate coefficients (both forward and reverse) relate to the energy barriers for the respective reaction halves and temperature in an Arrhenius fashion. For a typical thermally triggered reaction, energy barriers are related to the difference in energies between the metastable activated complex and reactant/product states. This mathematical form is shown in Eq. (5). For electrochemical reactions, the change in electrostatic potential jump across the electrified interface provides a means to alter the effective energy barriers as further shown in Eqs. (7,8) [1].

$$k(T) = k_0 e^{-\frac{E_A}{RT}} \tag{5}$$

where  $k_0$  is the pre-exponential factor,  $E_A$  is the activation energy of the reaction and R is the universal gas constant. Determining the reaction rate coefficients is often a challenge to modeling reactions, especially in electrochemical devices where multiple reaction steps and pathways exist. It is customary to describe electrochemical reactions in the form of current, rather than a molar rate, given the simplicity of current measurements. Thus, the molar rate as expressed in Eq. (4) is equivalent to an electrochemical current as shown in Eq. (6) [2]. The current associated with electrochemical reactions is also known as the Faradaic current (in contrast to the capacitive current associated with charge accumulation in a double layer) [3].

$$i_{e,F}(\vec{x}) = nF\left(k_{CT}^f \prod_{j}^{R,ct} c_j^{m_{fij}}(\vec{x}) - k_{CT}^r \prod_{j}^{P,ct} c_j^{m_{rij}}(\vec{x})\right)$$
 (6)

here,  $c_i$ ,  $m_{fij}$  and  $m_{rij}$  (keeping in mind the previous discussion on bulk species adsorption at the electrified interface) are as described before, F is Faraday's constant, n is the number of electrons. Depending on the participating species, the concentrations that contribute to the charge-transfer rate can be surface coverage, gas-phase compositions, or bulk-phase ion concentrations. The charge transfer reaction rates are defined as, [3]

$$k_{CT}^{f} = k_{f,CT}^{o} \exp\left(\frac{-E_{f,CT}^{act}}{RT}\right) \exp\left(-(1 - \alpha_{s})\frac{nF}{RT}\eta_{A}\right)$$
 (7)

$$k_{CT}^{r} = k_{r,CT}^{o} \exp\left(\frac{-E_{r,CT}^{act}}{RT}\right) \exp\left(\alpha_{s} \frac{nF}{RT} \eta_{A}\right)$$
 (8)

where  $\eta_A$  is the electrostatic potential difference, and  $\alpha_s$  is the electrode transfer coefficient. The jump in electrostatic potentials across the electrified interface do not necessarily contribute equally to both the forward and backward reactions. The asymmetry of this potential contribution is characterized by the charge transfer coefficient  $\alpha_s$  which in the limits of  $\alpha_s = 0.5$  provides equal contributions to both the halves.  $\alpha_s \to 1$  favors the backward reaction while  $\alpha_s \to 0$  favors the forward reaction.

It should be noted that the above discussion has been for elementary (i.e. single-electron charge transfer reactions) for which the charge transfer coefficients (symmetry factors) sum up to be unity. For multi-electron charge transfer reactions, the effective anodic and cathodic symmetry factors can vary greatly from elementary-reaction formulation. If the multiple electron transfer reaction mechanism can be broken down into multiple steps for single-electron transfer, kinetic parameters can still be determined, albeit with higher complications [4].

The current density is an implicit measure of the rate of electrochemical reactions since electrons are released through the electrochemical reactions. The Butler-Volmer equation, which can be derived independently from the theory of activated complexes as well as Marcus kinetics, is expressed as, [2,4–8]

$$i = i_0 \left[ \exp\left(\frac{-(1 - \alpha_s)nF\eta_A}{RT}\right) - \exp\left(\frac{\alpha_s nF\eta_A}{RT}\right) \right]$$
 (9)

where  $i_0$  is the exchange current density and  $\eta_A$  is the activation polarization. Note that the relation between the current density

(i) and the activation polarization ( $\eta_A$ ) is nonlinear and implicit, which does not allow for an explicit calculation of the activation polarization from the current density. Simplified expressions can be written for cases with high or low current density, such as the Tafel equation of the high current regime [9].

The Butler-Volmer relation can be used to calculate the local conditions within an electrochemical device by using a mesoscale electrochemistry approach [10,11]. The local Faradaic current density can be calculated from a local, modified Butler-Volmer relation as, [12]

$$i_{e,F}(\vec{x}) = i_{o,e}(\vec{x}) \left[ \exp\left(-\frac{(1-\alpha_s)F\eta_A(\vec{x})}{RT}\right) - \exp\left(\frac{\alpha_s F\eta_A(\vec{x})}{RT}\right) \right]$$
(10)

where  $i_{o,e}$  is the local exchange current density and  $\eta_A$  is the local activation polarization. The local activation polarization is calculated as,

$$\eta_A(\vec{x}) = \phi_s(\vec{x}) - \phi_e(\vec{x}) - U_{s,eq}(\vec{x})$$
 (11)

where  $\phi_s$  is the local potential of the electrode,  $\phi_e$  is the local electrolyte potential and  $U_{s,eq}$  is the local equilibrium potential of the electrode, which can be calculated using the Nernst equation with the local partial pressures of the gas.

Both the explicit formulation (Eq. (6)) for the current density and the implicit formulation (Eq. (10)) are used in mesoscale modeling of electrochemical devices.

#### 2.2. Charge transport

Charge transport in porous electrodes describes ionic transport in the electrolyte through the pore space. For example, in a typical LIB electrode, Li<sup>+</sup>ion transport in an inorganic electrolyte consisting of LiPF<sub>6</sub> salt and carbonate solvent, needs to be considered. A canonical representation of charge transport includes ionic concentration,  $C_i$ , related to ionic charge,  $q_i$ , and charge number,  $z_i$ , i.e.  $q_i = z_i F C_i$  (where F is Faraday's constant). Correspondingly, ionic flux based on the Nernst-Planck equation, can be expressed within the volume averaged porous medium representation as:

$$N_{i} = -D_{i} \frac{\varepsilon}{\tau} \nabla C_{i} - z_{i} F B_{i} \frac{\varepsilon}{\tau} C_{i} \nabla \phi_{e} + C_{i} \mathbf{u}$$
(12)

where  $D_i$  is the diffusion coefficient for the ion,  $\varepsilon$  is porosity, and  $\tau$  is tortuosity. The presence of a porosity/tortuosity ratio  $(\varepsilon/\tau)$  accounts for the transport resistance due to the porous network tortuosity.  ${\bf u}$  is a bulk (superficial) volume averaged velocity vector, which is often computed via Darcy's law for the volume averaged porous medium representation or else via the momentum conservation equation in a mesoscale representation. As discussed later in this review, mesoscale modeling is used to determine values of porosity and tortuosity within microstructures for use in Eq. (12); additionally Eq. (12) can be reformulated as a pore-scale model where the microstructure is explicitly resolved and the porosity and tortuosity do not need to be included.

The Nernst–Planck expression (Eq. (12)) represents ionic flux due to three mechanisms: (i) diffusion due to a concentration gradient  $\nabla C_i$ ; (ii) migration due to the electric potential gradient  $\nabla \phi_e$ ; and (iii) advection due to the solvent velocity field  $\mathbf{u}$ . Here  $B_i$  is ionic mobility and is related to ionic diffusivity via the Stokes-Einstein relation  $B_i = D_i/RT$  (R is universal gas constant and T is temperature). Using this flux description (Eq. (12)), the governing differential equation for ionic species transport in porous electrodes (volume-averaged) takes the form,

$$\varepsilon \frac{\partial C_i}{\partial t} + \nabla \cdot (\mathbf{u}C_i) = \nabla \cdot \left( D_i \frac{\varepsilon}{\tau} \nabla C_i \right) + z_i F \nabla \cdot \left( \frac{D_i}{RT} \frac{\varepsilon}{\tau} C_i \nabla \phi_e \right) + r_i$$

The electric field in the electrolyte (solution) phase  $\phi_e$  is described by the statement of charge conservation in the solution phase (Eq. (14)), where the source term  $J_j$  relates to the electrochemical reaction at the electrochemically active (solid/electrolyte) interface. Expressions for the effective ionic conductivity ( $\kappa^{eff}$ ) related to the potential gradient, and the effective diffusional conductivity ( $\kappa^{eff}_D$ ) related to the concentration gradient of the charged species are given in Eq. (15).

$$\nabla \cdot \left(\kappa^{eff} \nabla \phi_e\right) + \sum_i \left(\nabla \cdot \left(\kappa_{\scriptscriptstyle D}^{eff} \nabla C_i\right)\right) + \sum_i J_i = 0 \tag{14}$$

where.

$$\kappa^{eff} = \sum_{i} z_{i}^{2} F^{2} \frac{D_{i}}{RT} \frac{\varepsilon}{\tau} C_{i} 
\kappa_{D}^{eff} = z_{i} F D_{i} \frac{\varepsilon}{\tau}$$
(15)

Eq. (14) can be recast in terms of the total ionic flux  $I = \sum_{i} z_{i} F N_{i}$ 

$$-\nabla \cdot I + \sum_{i} J_{i} = 0 \tag{16}$$

Note that the electrochemical reaction source terms  $(J_j)$  are related to the species balance source terms  $(r_i)$  of Eq. (13) via reaction stoichiometry. Correspondingly, the charge conservation in the solid phase can be expressed as:

$$\nabla \cdot \left(\sigma^{eff} \nabla \phi_s\right) = \sum_j J_j \tag{17}$$

where  $\phi_s$  is the electric potential in the solid phase, and  $\sigma^{eff}$  is the effective electronic conductivity of the solid phase, which is determined from mesoscale models of the microstructure. The electric potentials,  $\phi_s$  and  $\phi_e$ , define the overpotential driving the electrochemical reactions at the electrochemically active (solid/electrolyte) interface. Note that if the porous medium is electronically insulating (e.g., a separator in LIBs), the solid phase potential equation is not required to be solved.

In summary, charge transport in a typical porous electrode requires a set of four governing equations: (1) species balance for charged species Eq. (13)); ((2) momentum equation for the solution phase (e.g., Darcy's law to obtain volume-averaged velocity field **u**; the effect of advection may be neglected in a typical LIB electrode.); (3) charge conservation in the solution phase Eq. (14)); and ((4) charge conservation in the solid phase (Eq. (17)). The solution of this set of coupled governing differential equations requires appropriate boundary and initial conditions.

## 2.3. Advection-diffusion-migration

The transport of species is central to the operation of electrochemical devices and includes the transport of reactants and products to/from the reaction sites. The transport of species can be divided into advective and diffusive transport. Advection is transport due to the bulk motion of a fluid; while diffusion is transport due to the random motion of molecules in a system. The transport of species can be described by the advection-diffusion equation,

$$\frac{\partial c_i}{\partial t} + \nabla \cdot (\vec{u}c_i) = \nabla \cdot J_i \tag{18}$$

where  $c_i$  is the molar concentration of species i,  $\overline{u}$  is the velocity and  $J_i$  is the diffusive molar flux of species i. Eq. (18) is coupled to the electrochemistry via a source term as discussed in Section 2.1 and Eq. (3).

Under certain conditions, advection or diffusion can be neglected without affecting the overall transport of species in the system, which allows for a simpler transport model. The relative

significance of advection and diffusion is determined by the Peclet number.

$$Pe = \frac{Lu}{D} \tag{19}$$

where L is the characteristic length of the system, u is the magnitude of the velocity and D is the diffusion coefficient [13]. When  $Pe\gg 1$  advection is the dominate transport mechanism and diffusion may be neglected; while if  $Pe\ll 1$  diffusion is dominate and advection may be neglected. Both advection and diffusion are significant when  $Pe\sim 1$ , in which case the full advection-diffusion equation should be solved.

Advection occurs when species are carried by the bulk flow of a fluid and is calculated from the velocity as shown in the second term on the left-hand side of Eq. (18). When advection is significant, the momentum conservation equation must be solved in addition to Eq. (18),

$$\rho \frac{\partial \vec{u}}{\partial t} + \rho \vec{u} \cdot \nabla \vec{u} = -\nabla P + \nabla \cdot (\mu \nabla \vec{u}) + F_{ext}$$
 (20)

where  $\rho$  is density, P is pressure,  $\mu$  is viscosity and  $F_{\textit{ext}}$  is any external forces such as gravity. The importance of advection to the operation of an electrochemical system must be considered on a case by case basis. In many multiphase electrodes, transport is dominated by diffusion and as such the advection within the electrode can be neglected. For instance in SOFCs, studies have shown that the effects of advection in the fuel and oxidant channels adjacent to the electrodes do not penetrate into the electrodes and transport can be assumed to be driven by diffusion within the electrodes [14]. However, in the fuel and oxidant channels above the electrodes advection is the dominant transport mechanism. Similarly in PEFCs, advection effects are critical to enhancing mass transport using an interdigitated channel design for the fuel and oxidant [15]. Additionally, in some electrochemical systems, advection is central to the system's operation, such as in flow batteries where the flow of electrolyte drives the power output of the battery.

The diffusive flux (*J*), which is the term on the right hand side of Eq. (18), is driven by the concentration gradients within the electrochemical device and is often a more difficult problem to formulate then advection. In many devices the electrodes are complex porous media. Diffusive transport within porous media can be a combination of molecular diffusion, Knudsen diffusion and surface diffusion. Molecular diffusion is the bulk diffusion of the fluid, which is due to the interactions of fluid molecules with other fluid molecules. Knudsen diffusion occurs in small pores where the pore radius is on the order of the mean free path of the fluid. Surface diffusion occurs when species that are adsorbed to the surface of the porous medium are mobile on the surface.

For molecular diffusion, the diffusive flux (J) is typically modeled as Fickian diffusion,

$$J_i = -D_{ij} \nabla c_i \tag{21}$$

where  $D_{ij}$  is the binary diffusion coefficient, which can be found from experimental data or calculated from theoretical and empirical relations [16]. Eq. (21) is formulated for a binary system, in systems with more than two species multi-component molecular diffusion occurs in which the effects of all species' interactions on diffusion must be accounted for. Under dilute conditions the system can be approximated as a binary system and can be modeled as Fickian diffusion [16]. In non-dilute cases, the Stefan-Maxwell equation can be used to describe multi-component diffusion [17,18],

$$-\nabla c_{i} = \sum_{\substack{j=1\\i \neq i}}^{n} \frac{N_{i}c_{j} - N_{j}c_{i}}{c_{T}D_{ij}}$$
(22)

where  $c_T$  is the total molar concentration of the mixture and  $N_i$  is the molar flux of species i relative to a stationary coordinate system.

In porous media, Knudsen diffusion can also be a significant transport mechanism. Knudsen diffusion occurs when the interactions of molecules with the pore walls become more frequent then the interactions of molecules with other fluid molecules. Knudsen diffusion is typically formulated as Fickian diffusion (Eq. (21)) with the Knudsen diffusion coefficient used in place of the binary diffusion coefficient. The Knudsen diffusion coefficient of a species is independent of the other species in the system and is derived from the molecular motion of the molecules and the geometry of the pores [16,19,20],

$$D_i^{Kn} = \frac{1}{3} d\sqrt{\frac{8RT}{\pi M_i}} \tag{23}$$

for a circular pore where d is the diameter of the pore, R is the universal gas constant and  $M_i$  is the molar mass of the gas species. In real porous media, such as the electrodes, the pore walls are rough and can have fractal internal surfaces which lead to more complicated formulations for the Knudsen diffusion coefficient [20]. Due to the difficulty in determining the diffusion coefficient in real pore geometries, ideal geometries such as spheres and cylinders are often used [19].

The significance of Knudsen diffusion is determined from the mean free path of the fluid and the pore diameter of the porous media. In a porous media with very small pores, Knudsen diffusion will dominate diffusive transport; while in systems with large pores, molecular diffusion will dominate. A transition region occurs in porous media with intermediate pore sizes where both Knudsen and molecular diffusion are significant.

In mesoscale computational models, the inclusion of both Knudsen and molecular diffusion can be a difficult task. Mesoscale models typically resolve the porous microstructure and depending on the size of a specific pore either Knudsen or molecular diffusion may be significant. In non-ideal systems it can be difficult to define individual pores and the appropriate pore diameter for each pore. Fig. 1 shows example microstructures seen in various electrochemical devices; the heterogeneity of the microstructure makes the identification of individual pores difficult. Often an effective diffusion coefficient is used to describe the combined effects of molecular and Knudsen diffusion or molecular diffusion is assumed to dominate the diffusive transport.

In addition to gas diffusion, surface diffusion may also be significant in electrochemical devices. Surface diffusion describes the mobility of molecules that are adsorbed to a surface. Surface diffusion can occur in systems with both physisorbed and chemisorbed species. When a species is physisorbed to a surface its adsorption energy is less than  $k_BT$  and the species are highly mobile. In chemisorption, where the adsorption energy is greater than  $k_BT$ , the species are more tightly bound to the surface and have less mobility but may still move by hopping from adsorption site to adsorption site on the surface [16]. Surface diffusion depends strongly on the temperature and surface conditions of the system. High temperatures, such as those found in SOFCs, have been shown to accelerate surface diffusion. Surface diffusion also increases with increasing surface concentrations; while different faces of a material can have drastically different surface diffusion rates [24]. Most surface diffusion models use the Fickian formulation (Eq. (21)) with a diffusion coefficient that is typically found through experimental measurements [25,26]. The surface diffusion coefficient is typically on the order of  $10^{-5}$  cm<sup>2</sup>/s but can vary widely for different materials and at different temperatures [16].

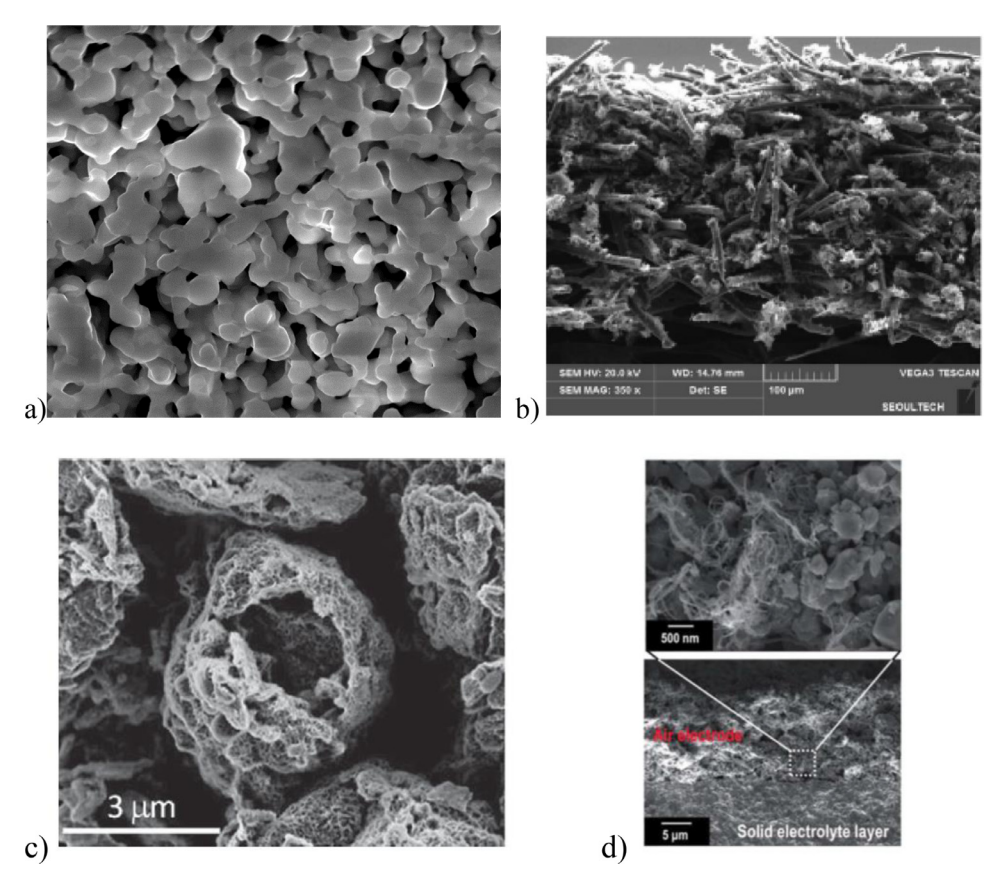


Fig. 1. Scanning electron microscopy (SEM) images of: (a) a porous SOFC cathode; (b) a SGL 10BA gas diffusion layer for PEFC (350 x magnification) [21]. Reproduced with permission from Elsevier; (c) a graphene air cathode for a Li-air battery Reprinted with permission from [22]. Copyright 2011 American Chemical Society; (d) a solid electrolyte-air electrode interface in a Li-air battery. Reproduced from [23] with permission of The Royal Society of Chemistry.

## 2.4. Heat transfer

Heat generation and thermal transport are extremely important for safe and optimal operation for electrochemical devices, including LIBs and PEFCs [27–29]. For example, non-uniform distribution and local excursion of temperature in the LIB is a safety concern for electric drive vehicles [27]. A generalized energy conservation equation for temperature distribution in a typical electrochemical device electrode can be expressed as [30–32],

$$\frac{\partial (\rho_k c_{p,k} T_k)}{\partial t} + \vec{u}_k \cdot \nabla (\rho_k c_{p,k} T_k) = \nabla \cdot (\lambda_k \nabla T_k) + q \tag{24}$$

where T is the temperature, q is the volumetric heat generation rate, and  $\rho$ ,  $c_p$ , and  $\lambda$  are density, specific heat, and heat conductivity, respectively, for each constituent phase, k. It is important to note that a typical electrode consists of multiple phases, for example the LIB electrode includes active material, conductive additive, binder and electrolyte. The thermophysical properties can be anisotropic due to the inhomogeneity of battery components. The convection due to electrolyte flow in the electrode is typically negligible and thermal conduction is the primary mode of heat transfer inside the cell.

The heat generation rate depends on the thermodynamic properties of the reactions proceeding in a cell, the potential-current characteristics of the cell, and the rates of charge and discharge. By utilizing the first law of thermodynamics for an isobaric battery system, Bernardi et al. [33] presented a general energy balance equation for a cell in which the rate of heat generation was given by:

$$q = \sum_{n} I_{n} \left( U_{n} - T \frac{\partial U_{n}}{\partial T} \right) - IV + \text{enthalpy of mixing term}$$
+ phase change term (25)

The first term on the right hand side of Eq. (25) represents the heat generated due to the enthalpy of the charge transfer reactions, the second term is the electrical work done by the battery. The first term is generalized for the nth reaction since an electrode also typically includes other side reactions leading to heat generation.  $I_n$  is the partial reaction current contribution from the nth electrode reaction,  $U_n$  is the corresponding open circuit potential, I is the apparent current density and V the cell potential. The enthalpy of mixing term represents the heat effect associated with concentration gradients in the cell and the last term represents heat effect due to phase transformations. The electrochemical-thermal coupling manifests in terms of temperature-dependent physicochemical properties (e.g. diffusion coefficient and ionic conductivity of the electrolyte) and dependence of the open circuit potential with local concentrations in the solid phase.

# 2.5. Distinction between direct numerical simulation and macrohomogeneous model

To summarize the electrochemical physics presented in the previous sub-sections, we present a fine-scale mathematical model of binary electrolyte intercalation chemistries-based LIBs with a fully resolved electrode-electrolyte interface alongside the requisite interface and boundary conditions. This example is used to expand on the concepts discussed earlier (direct numerical simulation (DNS)), and how boundary and initial conditions are applied to the governing equations of electrochemical physics. Furthermore, connection between the fully resolved DNS model and volume averaged macrohomogeneous model are established to provide a better understanding of the coupling between the modeling paradigms.

Lithium-ion battery physics encompasses species and charge transport in the electrolyte ( $Li^+$ ,  $PF6^-$ ) and electrode (Li,  $e^-$ ) phases alongside interfacial charge transfer at the electrode-electrolyte interface. The nature of the charge carrier changes at the electrode-electrolyte interface contributing to ionic current in the electrolyte phase (motion of  $Li^+$ ,  $PF6^-$ ) and electronic current (motion of  $e^-$ ) in the solid phase. For DNS on the fully resolved electrode-electrolyte structure this translates into the following set of coupled governing differential equations

Solid state diffusion: Li transport inside the solid active material particles is through diffusion under concentration gradients and Eq. (18) is solved (neglecting advection) with Fickian diffusion (Eq. (21)) to model transport inside the active material.

$$\frac{\partial c_s}{\partial t} = D_s \nabla^2 c_s \tag{26}$$

here,  $c_s$  is the concentration of Li atoms in the solid phase,  $D_s$  is the diffusivity of Li inside the solid phase and t is time.

*Li*<sup>+</sup> *transport in the electrolyte phase*: Diffusional transport under concentration gradients and migration under electric field contribute to *Li*<sup>+</sup> motion in the electrolyte phase.

$$\frac{\partial c_e}{\partial t} = \nabla \cdot (D_e \nabla c_e) + \frac{t^+ \nabla \cdot i_e}{F}$$
 (27)

here,  $c_e$  is the concentration of Li<sup>+</sup> ions in the pore phase electrolyte,  $D_e$  is the ionic diffusivity of  $Li^+$ ,  $t^+$  is the transference number which accounts for the fraction of ionic current,  $i_e$ , carried by  $Li^+$ . It should be noted that ionic current occurs through motion of both positive and negative charged species and hence fractional contributions of individual charged species appears in the species conservation equation. Additionally Eq. (27) is a variation of Eq. (13) for a mesoscopic domain.

*Electrolyte phase current:* The ionic current has contributions from electrolyte potential and concentration gradients.

$$i_e = -(\kappa \nabla \phi_e + \kappa_D \nabla \ln c_e) \tag{28}$$

here,  $\phi_e$  is the electrolyte phase potential,  $\kappa$  and  $\kappa_D$  are the ionic

and diffusional conductivity of the binary electrolyte respectively. *Charge conservation in the electrolyte phase (ionic current):* Conservation of ionic charge in the electrolyte phase leads to

$$\nabla \cdot (\kappa \nabla \phi_e + \kappa_D \nabla \ln c_e) = 0 \tag{29}$$

Charge conservation in the solid phase (electronic current): Electronic current is given using Ohm's law (only migration) and corresponding solid phase charge conservation takes the form

$$\nabla \cdot (\sigma \nabla \phi_{s}) = 0 \tag{30}$$

here,  $\sigma$  is the electronic conductivity of the solid phase and  $\phi_s$  is the electrostatic potential of the solid phase.

In addition to flux continuity, the above governing equations are coupled through the electrode-electrolyte interface via the following:

$$-D_s \nabla C_s \cdot \hat{n} = -D_e \nabla C_e \cdot \hat{n} = \frac{i}{F}$$
(31)

$$-\sigma \nabla \phi_{s} \cdot \hat{n} = -(\kappa \nabla \phi_{e} + \kappa_{D} \nabla \ln C_{e}) \cdot \hat{n} = i$$
(32)

where  $\hat{n}$  is the local surface normal pointing from the solid phase towards the electrolyte phase, and i is Butler–Volmer current density as given by Eq. (9). It is apparent that the electrochemical reaction terms appear as interface conditions in the DNS formulation. The boundary conditions at the solid-phase current collector interface will be given by

$$-\sigma \nabla \phi_{s} \cdot \hat{n} = -(\kappa \nabla \phi_{e} + \kappa_{D} \nabla \ln C_{e}) \cdot \hat{n} = i_{app}$$
(33)

where  $i_{app}$  is the applied current density for the system. It should be noted here that the exchange current density for Li-ion based

intercalation chemistries shows functional dependence on the solid phase concentration at the particle surface and electrolyte phase concentration given by [32]

$$i_0 = k \left( c_s^f c_e (c_s^{max} - c_s^f) \right)^{1/2}$$
 (34)

here, k is the rate constant,  $c_s^f$  is the surface concentration of Li in the solid phase and  $c_s^{max}$  is the maximum amount of Li that can intercalated in the solid phase.

From the above discussion, it is clear that the electrochemical charge transfer reactions proceeding at the electrode-electrolyte interface appear as interfacial or boundary conditions for the fully resolved DNS model. With an appropriate set of initial conditions, the above formulation is well-defined to obtain the temporal and spatial evolutions of the concentration and potential fields inside the LIB. However, this approach enforces a huge amount of computational burden and requires the fully resolved electrode microstructure geometry.

Alternatively, if an electrode-electrolyte assembly is homogenized and represented as a composite material, then a sourceterm representation can be developed as is seen for the volume averaged macrohomogeneous models. Through homogenization of the porous electrode microstructure, volume averaged quantities are obtained with the primary parameters of consequence being porosity  $\varepsilon$ , pore phase tortuosity  $\tau$ , active material-electrolyte specific surface area  $a_s$  and effective electronic conductivity of the solid phase  $\sigma^{eff}$ . Porosity accounts for the fraction of void space in the porous electrode while tortuosity is a measure of the convolutedness of the transport pathways inside the porous electrode. The interfacial electrochemical reactions occur at the electrolyte-active material interface; hence, the corresponding surface area is an important descriptor for the electrode-electrolyte assembly. Finally, the effective electronic conductivity is a measure of the electronic conductivity of the composite solid phase microstructure consisting of active material and secondary inclusions. The effective pore phase transport parameters can then be obtained through the following relations:

$$D_{e,eff} = D_e \frac{\varepsilon}{\tau}, \quad \kappa_{eff} = \kappa \frac{\varepsilon}{\tau}, \quad \kappa_D^{eff} = \kappa_D \frac{\varepsilon}{\tau}$$
 (35)

Correspondingly, the macrohomogeneous model for the LIB consists of the following set of governing differential equations (variables being the same as described for the DNS model):

Solid state diffusion:

$$\frac{\partial c_s}{\partial t} = D_s \nabla^2 c_s \tag{36}$$

Li<sup>+</sup> transport in the electrolyte phase:

$$\varepsilon \frac{\partial c_e}{\partial t} = \nabla \cdot \left( D_{e,eff} \nabla c_e \right) + \left( 1 - t^+ \right) \frac{a_s i}{F} \tag{37}$$

Charge conservation in the electrolyte phase (ionic current):

$$\nabla \cdot \left( \kappa_{eff} \nabla \phi_e + \kappa_{D,eff} \nabla \ln c_e \right) + a_s i = 0 \tag{38}$$

Charge conservation in the solid phase (electronic current):

$$\nabla \cdot (\sigma_{\text{eff}} \nabla \phi_{\text{s}}) = a_{\text{s}} i \tag{39}$$

It should be noted that the homogenized governing differential equations contain microstructure properties as well as source terms similar to Eq. (3). Herein lies the difference between the macrohomogeneous and DNS models. While, the interfacial electrochemical reactions present as interface terms in the DNS model, the effective medium approach of a macrohomogeneous model is able to treat the interfacial reactions as source terms in the governing differential equations. The corresponding boundary conditions for the macrohomogeneous model are enumerated below as well.

Variable	Anode – current collector boundary	Anode – separator boundary	Cathode – separator boundary	Cathode – current collector boundary
$\phi_a$ $\phi_c$	$i_{app} = -\sigma_a^{eff} \nabla \phi_s$	$\nabla \phi_s = 0$	$ \nabla \phi_s = 0 $	$-i_{app} = -\sigma_s^{eff} \nabla \phi_s$
$\phi_e$	$\nabla \phi_e = 0$ $\nabla c_e = 0$	$\kappa_{eff} \nabla \phi_e + \kappa_{D,eff} \nabla \ln c_{e\vec{x}^-} $ $= \kappa_{eff} \nabla \phi_e + \kappa_{D,eff} \nabla \ln c_e _{x^+} $ $D_{eff} \nabla c_e _{\vec{x}^-} = D_{eff} \nabla c_e _{x^+} $	$\kappa_{eff} \nabla \phi_e + \kappa_{D,eff} \nabla \ln c_{e\vec{x}^-} $ $= \kappa_{eff} \nabla \phi_e + \kappa_{D,eff} \nabla \ln c_e _{x^+} $ $D_{eff} \nabla c_e _{\vec{x}^-} = D_{eff} \nabla c_e _{x^+} $	$\nabla \phi_e = 0$ $\nabla c_e = 0$

#### 3. Mesoscale modeling methods

Mesoscale modeling methods focus on resolving the chemical-physical processes occurring within porous microstructures and at interfaces and surfaces within electrochemical devices. There are two broad categories of computational methods used to simulate mesoscale phenomena in electrochemical devices, particle-based methods, and mesh based or fine-scale computational fluid dynamics (CFD) methods. In both methods, the microstructure of interest needs to be defined *a priori* and is an input to the model. In the following sub-sections we describe methods of microstructure representation, the fundamentals of various mesoscale modeling methods along with notable results and some of the challenges of using these methods.

#### 3.1. Porous microstructure representation

Mesoscale modeling of electrochemical systems requires the geometrical details of the microstructure, such as a porous electrode, as input. Naturally, the accuracy of pore-scale calculations is directly tied to the fidelity of microstructural information. Realizations of porous microstructures can be obtained either by experimental imaging or by stochastic reconstruction methods.

# 3.1.1. Experimental imaging

There are two main experimental methods for imaging 3D porous microstructures, X-ray computed microtomography (XCT) and focused ion beam—scanning electron microscopy (FIB-SEM) [34]. In recent years, there has been tremendous progress in XCT [35,36,45–47,37–44] based 3D porous structure reconstruction, which is a non-invasive experimental technique. FIB-SEM [48–52] is a destructive technique that uses a focused ion beam to slice the sample plane-by-plane while simultaneously imaging each of these planes. The XCT technique uses X-rays, which have much smaller wavelengths than the visible light and proffer sufficient resolution. On the other hand, FIB-SEM relies on accelerated electrons that exhibit a wave nature (de Broglie waves). The wavelength of the associated waves is inversely related to the square

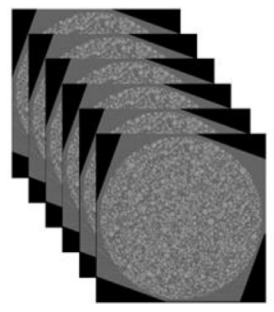
root of the accelerated voltage and equivalently the wavelength could be made small enough to probe microstructural attributes. These two techniques are quite different in terms of the probe (X-ray energy vs. electron waves), interaction with the sample, and interpretation of the contrast data. X-rays penetrate solids, while electrons do not. Current XCT technology does not provide enough contrast with respect to some materials, e.g., carbon additives and polymeric binder domains in LIB electrodes, while FIB-SEM is more restrictive in terms of the field of view. At the end of the experiment, these contrast images are analyzed to reconstruct porous electrodes. A typical workflow for XCT is shown in Figs. 2, and 3 provides an illustration of the multi-scale nature of the FIB-SEM technique.

#### 3.1.2. Stochastic reconstruction

Stochastic reconstruction, on the other hand, is quite an efficient approach to study a wide variety of electrode microstructures with different compositions, porosities, particle types, etc. Additionally, it allows one to generate large enough domains (unlike FIB-SEM) containing all the relevant phases (unlike XCT). In other words, stochastic reconstruction can be suitably used to circumvent the limitations of imaging techniques as and when required.

For the reconstructed microstructures to represent realistic electrodes, generation routines often march (evolve the structure) to match statistical details of experimental structures, e.g., phase fractions, contact probability, 2-point correlation function, etc. [53,54]. Such techniques must guarantee connectivity of the solid phases (active material, conductive additive and binder taken together) for efficient electronic conduction in the electrode, for the resulting microstructural realizations to be of practical significance.

3.1.2.1. Monte Carlo (MC). Monte Carlo modeling [55–59] for microstructure regeneration is based on random number generators and statistical distributions. First particle dimensions and orientations are specified in the form of statistical distributions. Then particle locations are randomly generated till the particle volume fraction equals the prescribed value. Particle overlap is allowed to



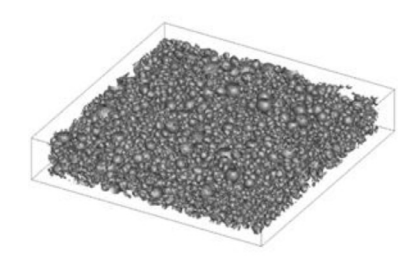
(a) X-ray Tomography Images



(b) Cropped Images



(c) Segmented Images



(d) Reconstructed Microstructure

Fig. 2. Image processing steps translate raw image data into 3D microstructural reconstruction of porous electrodes. The raw images (a) are first aligned with respect to each other so the same pixel on successive images correspond to identical in-plane locations on the electrode and then cropped to isolate the region of interest (b). At this stage other corrective steps are applied such as filtering. Next the images are segmented to identify material phases (c), and eventually these are combined together to give a 3D reconstruction (d). The images in (a) to (c) are obtained from open source XCT data for a LIB cathode [47], while (d) is reconstructed from corresponding segmented image slices.

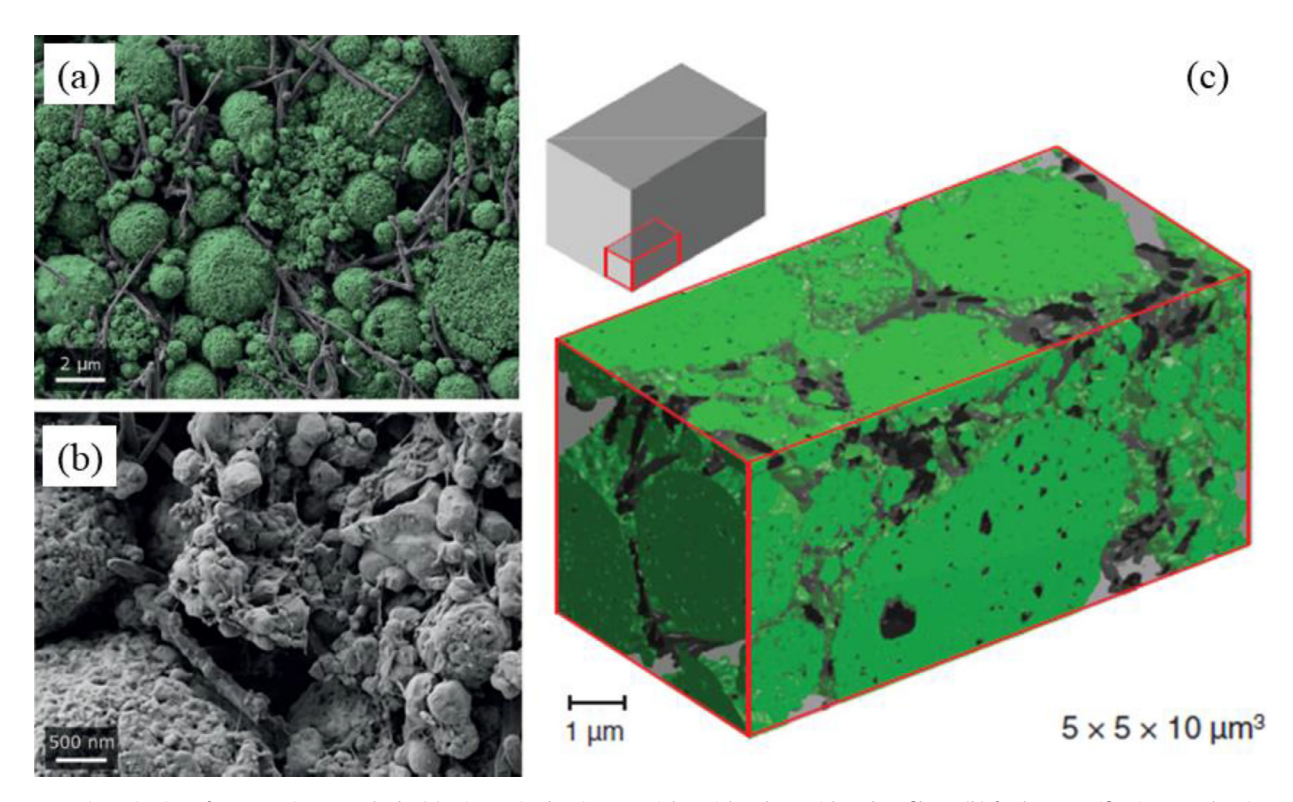


**Fig. 3.** FIB-SEM investigation of a composite LIB cathode. (a) Micron-sized active material particles along with carbon-fibers; (b) further magnification reveals primary active material particles of a couple hundred nanometers; (c) 3D electrode reconstruction; inset shows the location of the reconstructed portion compared to the electrode sample. Reproduced from [49] with permission of the Electrochemical Society. Copyright 2012, The Electrochemical Society.

guarantee solid phase connectivity for efficient electronic conduction. The same procedure can be extended to incorporate multiple solid phases.

3.1.2.2. Dynamic particle packing (DPP). This approach [53,60] is derived from molecular dynamics simulations. Here active material, conductive additive and binder particles are randomly distributed as per user-specified volume fractions. The system is evolved in time till its minimum energy state is reached (i.e., equilibrium state) based on suitable interparticle force descriptions. The active particles are modeled as hard spheres while conductive additive and binders are treated as soft spheres to ensure connectivity of the solid phase. The method can be easily extended to work with non-spherical particulate matter, if the functional nature of the force field is available. For the reconstruction to be more realistic, experimental particle size distributions are used instead of having monodisperse particles.

3.1.2.3. Stochastic grid. This approach is quite closely related to Monte Carlo generation [43,51,53]. In this method, a possible microstructure is generated by randomly placing solid phase particles. Then multiple successive realizations are obtained by swapping neighboring particles (thus maintaining volume constancy) till the statistical function of the generation structure (e.g., 2-point correlation function) matches the experimentally obtained value. Alternatively the system can also be driven to a minimum state of energy. As the microstructure is randomly generated, ensuring particle connectivity becomes a challenge, unless particle overlap is allowed.

3.1.2.4. Simulated annealing. This algorithm starts with a random configuration of particulate phases [61,62]. Energy is defined in terms of an objective statistical descriptor (here energy is used in a generic sense). Then successive new structures are generated by

shifting particle locations. The new particle location is accepted or rejected based on a probabilistic rule. Thus, every new microstructure is closer to the desired state and eventually converges after a finite number of operations.

3.1.2.5. Controlled random generation / quasi-random generation. Such a procedure grows electrode structure sequentially [63,64]. First random seeds are chosen, and active particles are grown around them to meet the desired volume fraction. Due to the random seed initiation, the generated phase tends to be well connected as the volume fraction is increased. Once, the active material is grown, conductive additive and binder are selectively grown on active material surfaces, thus further ensuring solid phase connectivity. Due to this selective nature, the technique is referred to as controlled random generation or quasi-random generation.

3.1.2.6. Applications of stochastic reconstruction to electrochemical systems. Recently a novel physics-based description was developed to add secondary (non-intercalating) solids in the active material backbone for LIB electrodes, Fig. 4 [65]. This not only allows one to reconstruct composite electrode structures with all the essential details but also helps delineate physicochemical limitations arising from microstructural complexations. Future efforts should harness the lucrative aspects of stochastic reconstructions in order to extend the scope of imaging techniques as well as foster a holistic view of composite electrode structures.

Similarly, stochastic microstructure generation methods have received significant attention in the PEFC, namely for the reconstruction of the porous catalyst layer (CL), microporous layer (MPL) and fibrous gas diffusion layer (GDL) [54,66,67]. 3-D realization of the non-woven carbon paper GDL was reconstructed based on structural inputs (fiber diameter, fiber orientation and porosity), which can be obtained either directly from the fabrication specifications or indirectly from the SEM (scanning electron micro-

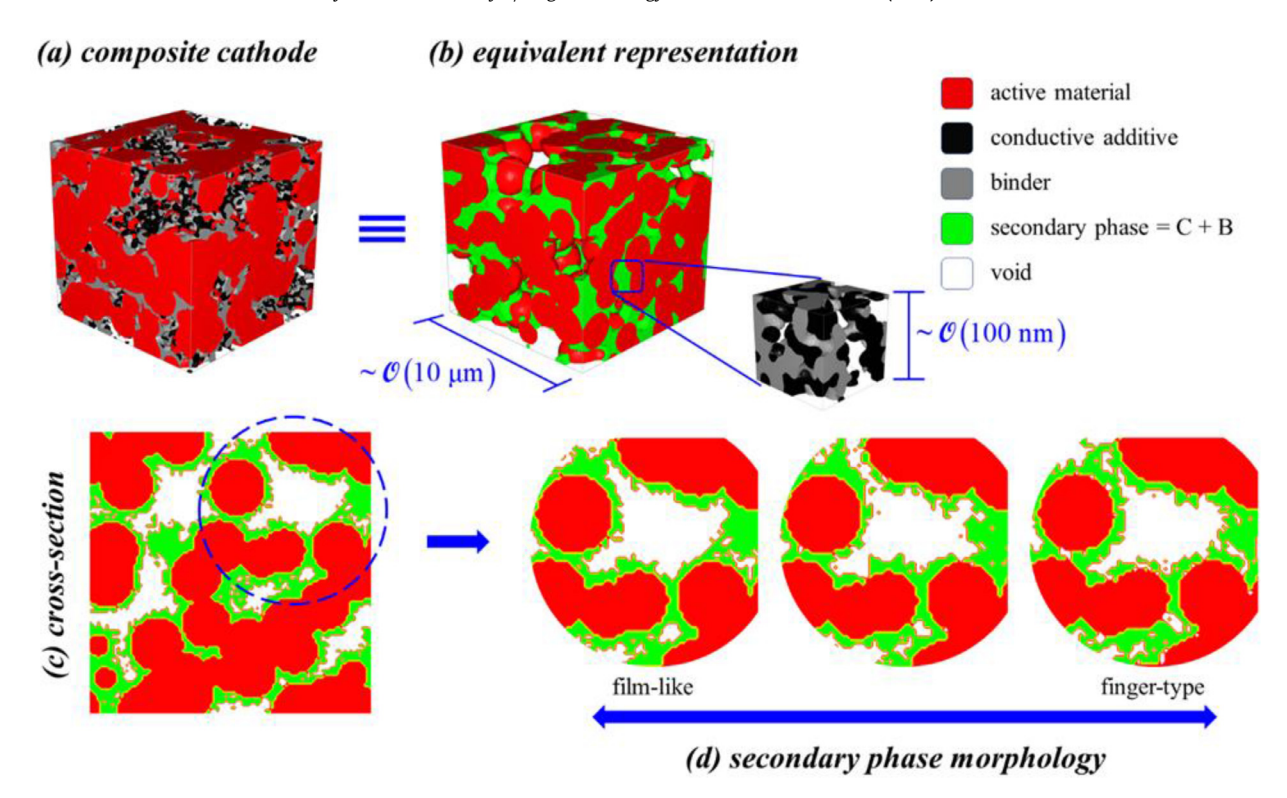


Fig. 4. Stochastic reconstruction of battery electrodes. (a) These composite electrodes have multiple phases with often hugely varying length scales, which allows one to treat the smaller sized solids as a secondary phase (b). This secondary phase can adopt different interfacial arrangements, i.e., morphologies based on electrode fabrication processes. These morphologies could range from a film-type coating to a finger-like arrangement. Reprinted with permission from [65]. Copyright 2018 American Chemical Society.

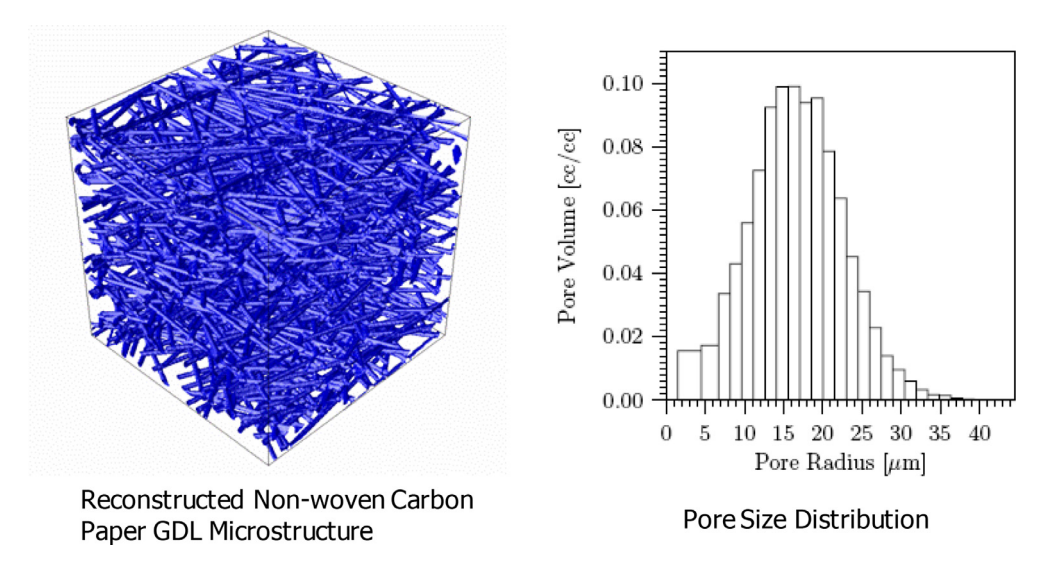


Fig. 5. Stochastic reconstruction of a typical fibrous GDL in PEFC. Reproduced from [67] with permission from the Journal of the Electrochemical Society. Copyright 2007, The Electrochemical Society.

scope) micrographs or by experimental techniques. This reconstruction method is a highlight of the GeoDict software [68]. Fig. 5 shows a representative reconstructed microstructure of a typical non-woven, carbon paper GDL [67] with porosity around 72% and thickness of 180  $\mu$ m along with the pore size distribution.

#### 3.2. Particle methods

Various particle-based numerical methods have been used to model the multiphase physics of electrochemical devices, such as reactive transport, heat transfer and solid mechanics. These methods include dissipative particle dynamics (DPD), smoothed particle hydrodynamics (SPH), discrete element methods (DEM), and the Lattice Boltzmann method (LBM). DPD, SPH and DEM methods are all considered off-lattice methods, where the domain is represented by Lagrangian particles, which move throughout the system due to the forces acting on them. In these methods, there is no grid or mesh used in the simulation domain. The LBM represents the domain as a collection of pseudo-particles, which interact via propagation and collision on a discrete lattice domain structure. In all particle methods each particle carries its physical properties with it (i.e. temperature, density, concentrations, etc.) and evolves over

time based on interactions with neighboring particles, which are calculated based on a weighted interaction term. The exact form of a particle's interactions with neighboring particles is what distinguishes one method from another.

Although all of these methods have been used to model fuel cells, batteries and other electrochemical devices; SPH, DPD, and LBM are the most widely used for mesoscale modeling of electrochemical devices and will be the focus of this section.

#### 3.2.1. Smoothed particle hydrodynamics fundamentals

In smoothed particle hydrodynamics (SPH) particles are used as interpolation points to discretize and solve the governing partial differential equations of a system based on the SPH smoothing function (kernel). The SPH method is based on the integral interpolation scheme for a continuous field, A [69]

$$A_{s}(\vec{x}) = \int A(\vec{x})W(\vec{x} - \vec{x'}, h)d\vec{x'}$$

$$\tag{40}$$

where  $A_s$  is the smooth approximation of A, W is the SPH kernel with a support length of h and the integration is performed over the entire domain of A. The kernel, W, is chosen such that it is differentiable, normalized over the volume,

$$\int_{\Omega_{c} \cup \Omega_{c}} W(\vec{x'} - \vec{x}, h) d\vec{x'} = 1 \quad \vec{x} \in \Omega_{P} \cup \Omega_{S}$$

$$\tag{41}$$

and tends towards the delta function as  $h \rightarrow 0$ . When W is the delta function Eq. (40) reproduces A exactly [69].

In the SPH method, the computational domain is discretized with a set of particles, and the integral, Eq. (40), is approximated as the summation:

$$A_{s}(\vec{x}) = \sum_{i} \frac{m_{i}}{\rho_{i}} A_{i} W(\vec{x} - \vec{x}_{i}, h) = \sum_{i} \frac{A_{i}}{d_{i}} W(\vec{x} - \vec{x}_{i}, h), \tag{42}$$

where  $\vec{x_i}$  is the position of particle i,  $A_i = A(\vec{x_i})$ ,  $d_i = \frac{\rho_i}{m_i}$  is the particle number density (number of particles per volume),  $\rho_i$  is the fluid density and  $m_i$  is the mass of particle i and  $\sum_i$  assumes summation over all particles [69]. In general, the summation in Eq. (42) is over all particles but due to the form of the kernel only particles within a distance h from the particle of interest will have a non-zero contribution to the sum and need to be included in the summation in the numerical implementation of a SPH method. This greatly reduces the computational cost of SPH simulations.

Since the SPH kernel is differentiable, the gradient of  $A_s$  can be written as [69]

$$\nabla A_s(\vec{x}) = \sum_i \frac{A_i}{d_i} \nabla_i W(\vec{x} - \vec{x_i}, h)$$
(43)

Using the SPH formulation of a field (Eq. (42)) and its derivative (Eq. (43)) the partial differential equations of a system can be written in SPH form. SPH has many attractive features, which provide it with an advantage over finite difference and finite element models for problems involving geometrically complex domains and/or surface interactions. The meshless discretization of SPH allows the conservation equations to be solved in the Lagrangian framework. The particle nature of SPH permits easy implementation of physical and chemical effects within advection modeling. SPH also explicitly conserves mass and linear momentum and due to its Lagrangian nature does not require explicit boundary tracking, which allows for simple implementation of complex geometries and/or moving boundaries [70]. SPH also has a number of disadvantages, which have limited its application, some of these include the implementation of boundary conditions, discretization error, and convergence and stability issues under high parameter gradients. These are all active areas of research within the SPH community [71]. SPH was originally developed for astrophysical systems [72,73] and

has since been applied to a variety of fluid dynamics and reactive transport problems [70,74–77]. Recently, SPH models have been developed to investigate the complex physics of electrochemical devices, including the operation and degradation of both fuel cells and batteries [78–82].

# 3.2.2. Dissipative particle dynamics fundamentals

Dissipative particle dynamics (DPD) is a mesoscale particle-based method, which simulates hydrodynamics and thermal fluctuations. It was originally developed by Hoogerbrugge and Koelman [83] and formulated as a statistical mechanics model by Español and Warren [84]. The change in position  $(r_i)$  and velocity  $(v_i)$  of particles are governed by Newton's equations of motion,

$$\frac{dr_i}{dt} = v_i 
\frac{dv_i}{dt} = \frac{f_i}{m}$$
(44)

where the force  $(f_i)$  between particles are governed by three pairwise forces [85],

$$f_i = \sum_{j \neq i} \left( F_{ij}^C + F_{ij}^D + F_{ij}^R \right) \tag{45}$$

The conservative force ( $F^{C}$ ) is a soft repulsion force, which acts between the center of masses of two particles, with the simple form [86],

$$F_{ij}^{C} = \sum_{j \neq i} \alpha_{ij} \left( 1 - \frac{r_{ij}}{r_c} \right) \hat{r}_{ij} \tag{46}$$

where  $r_{ij}$  is the distance between particles i and j,  $r_c$  is a cutoff radius beyond which the force between particles is zero,  $\alpha_{ij}$  is a particle interaction coefficient, and  $\hat{r}_{ij}$  is the unit vector.

The dissipative force  $(F^D)$  and stochastic force  $(F^R)$  constitute a pair-wise Brownian dash-pot model and represent the viscous and thermal noise between particles, respectively [86]. Both forces include a "bell-shaped" weighting function to model the particle interactions and  $F^R$  also includes a stochastic term, such as a Wiener Process, to introduce randomness. Common formulations for the dissipative and stochastic forces are [86],

$$F_{ij}^{D} = \sum_{i \neq i} \gamma w^{D}(r_{ij}) (\nu_{ij} \cdot \hat{r}_{ij}) \hat{r}_{ij}$$

$$\tag{47}$$

$$F_{ij}^{R} = \sum \sigma w^{R}(r_{ij}) \frac{dW_{ij}}{dt} \hat{r}_{ij}$$
(48)

where  $v_{ij}$  is the relative velocity between particles i and j,  $\gamma$  is a friction coefficient,  $w^D$  and  $w^R$  are the dissipative and random weighting functions, respectively, which are a function of the distance between particles  $(r_{ij})$  and have a support length of  $r_c$ ,  $\sigma$  is related to  $\gamma$  by  $\sigma^2 = 2\gamma k_B T$  where  $k_B$  is the Boltzmann constant and T is temperature, and  $dW_{ij}$  is an independent increment of the Wiener process [85,86].

DPD has been used as a method for upscaling molecular dynamics (MD) scale simulations and a bridge between coarse grain MD and continuum CFD models [87]. However, DPD has several limitations, which need to be considered when using the method. These limitations include the inability to specify thermodynamics behavior as an input, for instance the model can be fit to the compressibility of a fluid but in doing so may cause the predicted pressure to be unrealistic. The dissipative nature of the method does not allow temperature gradients to be sustained. For multiphase flows, DPD will not capture the drag between neighboring particles unless it has a radial velocity component. The formulation is hardwired to scale such that changing the number of particles in the system requires reparametrizing the system, i.e. there is no such

thing as convergence or grid refinement in DPD. Finally, the thermal fluctuations of DPD are not a function of volume or size and as such do not scale with the system. Modifications to the original DPD formulation have been implemented to overcome some of the limitations of the model [86]. The fluid particle model (FPM) adds a shear force to DPD that depends not only on the approaching velocity but also on the velocity difference, which overcomes the simplistic friction forces of DPD. Further modifications have led to the smoothed DPD method, which is based on an SPH formulation and includes a thermal fluctuation term that scales with size [86].

#### 3.2.3. Lattice Boltzmann method fundamentals

The lattice Boltzmann method (LBM) is a particle-based, mesoscopic approach with a simplified kinetic description based on classical statistical physics. Within the LBM framework, a fluid is represented as a collection of pseudo-particles and interacts via propagation and collision on a discrete lattice domain structure. The LBM is inherently a scale-bridging numerical scheme, which incorporates simplified kinetic models to capture microscopic flow physics, and the ensemble-averaged quantities satisfy the macroscopic behavior [88]. Due to the underlying kinetic nature, the LBM has received wide acceptance in fluid flow applications involving interfacial dynamics and complex boundaries, e.g. multiphase/multicomponent flows in porous medium [88]. In the context of electrochemical devices, the LBM has received significant interest in investigating the underlying physicochemical and twophase transport behavior in the constituent microporous components in fuel cells [54].

The two-phase LB modeling algorithms, reported in the literature, and variants thereof, include the model by Gunstensen et al. [89], Shan and Chen [90,91], Swift et al. [92,93], and He et al. [94]. Among these two-phase LB models, the model by Shan and Chen [90,91] is widely used due to its simplicity in implementing boundary conditions in complex porous structures, versatility in handling fluid phases with different densities, viscosities and wettabilities, as well as the capability of incorporating different equations of state.

In brief, the Shan and Chen model introduces k distribution functions for a fluid mixture comprising of k components. Each distribution function represents a fluid component and satisfies the evolution equation. The non-local interaction between particles at neighboring lattice sites is included in the kinetics through a set of potentials. The evolution equation for the kth component can be written as:

$$f_i^k(\mathbf{x} + \mathbf{e}_i \delta_t, t + \delta_t) - f_i^k(\mathbf{x}, t) = -\frac{f_i^k(\mathbf{x}, t) - f_i^{k(eq)}(\mathbf{x}, t)}{\tau_k}$$
(49)

 $f_i^k(\mathbf{x},t)$  is the number density distribution function for the kth component in the ith velocity direction at position  $\mathbf{x}$  and time t, and  $\delta_t$  is the time increment. In the term on the right-hand side,  $\tau_k$  is the relaxation time of the kth component in the lattice unit, and  $f_i^{k(eq)}(\mathbf{x},t)$  is the corresponding equilibrium distribution function. The right hand side of Eq. (49) represents the collision term based on the BGK (Bhatnagar–Gross–Krook), or the single-time relaxation approximation [95]. The spatio-temporal discrete form of the LB evolution equation based on the BGK approximation, given by Eq. (49), is often referred to as the LBGK equation. A typical 3-D 19-speed lattice (D3Q19, where D is the dimension and Q is the number of velocity directions), with the velocity directions, is shown schematically in Fig. 6.

The phase separation between different fluid phases, the wettability of a particular fluid phase to the solid, and the body force, are taken into account by modifying the velocity used to calculate the equilibrium distribution function. An extra component-specific

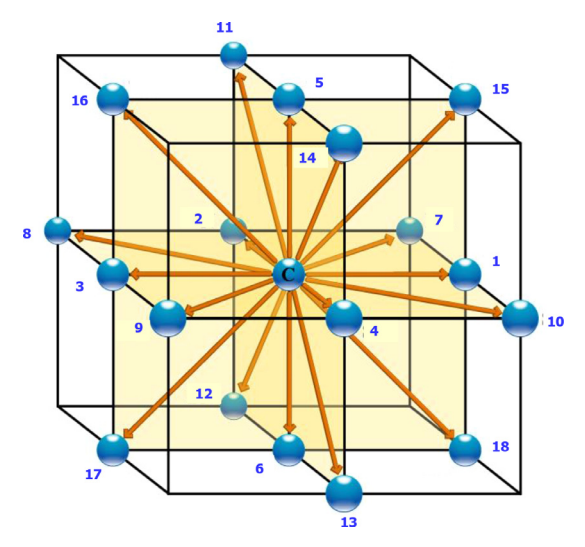


Fig. 6. Schematic of a typical D3Q19 lattice structure [96].

velocity due to interparticle interaction is added on top of a common velocity for each component. Interparticle interaction is realized through the total force,  $\mathbf{F}_k$ , acting on the kth component, including fluid/fluid interaction, fluid/solid interaction, and external force. More details can be found in the reference [97].

The continuity and momentum equations can be obtained for the fluid mixture as a single fluid using the Chapman–Enskog expansion procedure in the nearly incompressible limit:

$$\frac{\partial \rho}{\partial t} + \nabla \cdot (\rho \mathbf{u}) = 0$$

$$\rho \left[ \frac{\partial \mathbf{u}}{\partial t} + (\mathbf{u} \cdot \nabla) \mathbf{u} \right] = -\nabla p + \nabla \cdot [\rho \nu (\nabla \mathbf{u} + \mathbf{u} \nabla)] + \rho \mathbf{g}$$
(50)

where the total density and velocity of the fluid mixture are given, respectively, by:

$$\rho = \sum_{k} \rho_{k}$$

$$\rho \mathbf{u} = \sum_{k} \rho_{k} \mathbf{u}_{k} + \frac{1}{2} \sum_{k} \mathbf{F}_{k}$$
(51)

with a non-ideal gas equation of state [98].

The primary physical parameters, such as the fluid/fluid and fluid/solid interaction parameters, need *a priori* evaluation through model calibration using numerical experiments. The fluid/fluid interaction gives rise to the surface tension force and the fluid/solid interaction manifests in the wall adhesion force. The fluid/fluid and fluid/solid interaction parameters are evaluated by designing two numerical experiments, the *bubble test* in the absence of the solid phase and the *static droplet test* in the presence of a solid wall, respectively. The details of these numerical experiments are detailed elsewhere [97,99,100].

#### 3.2.4. Notable results

Particle-based modeling methods have been used to investigate reactive transport within multiphase regions of electrochemical devices. In particular studies have considered the effects of microstructure on the wettability, water transport and proton conduction of PEFCs [101–105], multiphase transport of the electrolyte in vanadium flow batteries [106,107], effects of electrode structure on LIB performance and thermal characteristics [81,108–112] and porous reactive transport and degradation in SOFC electrodes [80,113–121]. Here we will highlight some of the notable results from these studies and direct the reader to the references for further details.

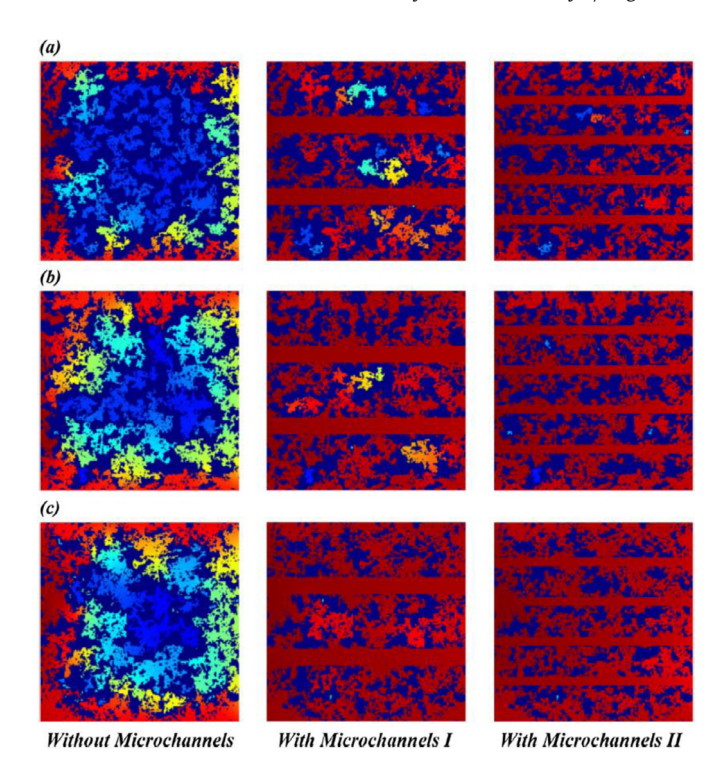


**Fig. 7.** Wettability of a porous electrode without microchannels and with two different microchannel designs for porosities of (a) 0.4, (b) 0.5, (c) 0.6. Reprinted from [108] with permission from Elsevier.

The effects of microstructure and changes to the microstructure are critical areas of research for mesoscale models across battery and fuel cell technologies. The ability of particle-based methods to easily handle complex and changing geometries has lead them to be used in a number of studies considering the effects of mesoscale microstructure and heterogenities on device performance. Changes to the porosity, tortuosity, pore size and pore distribution can be used to tune the performance of electrodes, such as in LIB electrodes where the porous structure is critical to the wettability of the liquid electrolyte and therefore the battery performance. Lee at al use LBM simulations to show that the porous microstructure can lead to pore blockage and resistance that decreases wettability and performance, highlighting the need for careful design of electrode microstructures [102]. Mohammadian and Zhang expanded on Lee et al.'s findings and use LBM to investigate the use of microchannels in LIB electrodes to improve wettability and prevent thermal runaway, Fig. 7 [108].

Particle-based methods have also been used to explore the effects of mesoscale heterogeneties and have shown that inclusion of the microstructrue is critical to understanding device performance. He et al investigated the effects of isotropic vs. anisotropic microstructural properties in the cathode of an SOFC using LBM [116]. Their work focused on the development of a multi-scale modeling apporach where a LBM sub-grid model of reactive transport in the cathode microstructure is coupled with a coarse finite element model (FEM) of overall battery performance. Their work showed the importance of accounting for mesoscale heterogenities for the accurate prediction of SOFC performance, in particular accurately capturing heterogeneous diffusion lead to more accurate predictions of electrode tortuosity.

Tan et al. used a mesoscale SPH model to investigate the effects of anisotropic mass transfer near the anode-electrolyte interface in Li-air batteries for the study of dendrite growth [81,112,122]. Their work showed that controlled mass transport could be an effective strategy for suppressing dendrite growth in Li-air batteries. Addi-

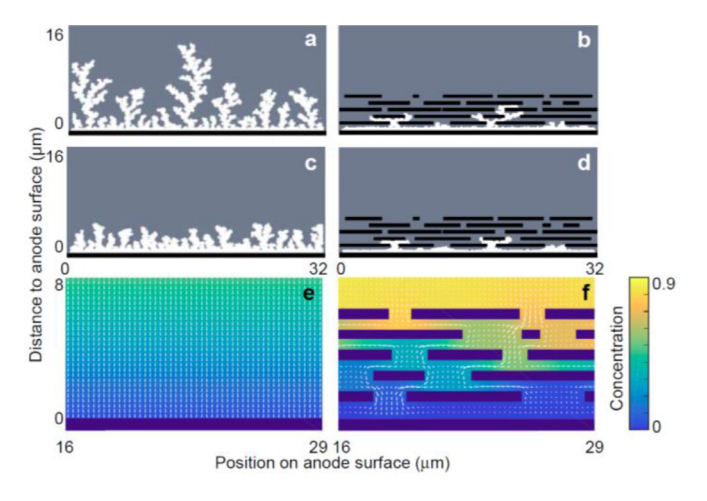


**Fig. 8.** The effects of a separator on dendrite growth at the anode-electrolyte interface in a Li-air battery. Reprinted with permission from [82]. Copyright 2018 American Chemical Society.

tionally they showed that restricted mass flux and increased tortuosity in seperators can restrict mass transport enough to reduce dendrite growth, Fig. 8, and validiated their models with experimental data [82,112]. Tan et al.'s work shows the use of mesoscale models not just for model development but for improved battery performance and design of new battery microstructures. Taking mesoscale models from simply the academic and computational science realm and into the experimental and design realm will help to accelerate development of electrochemical devices.

Two-phase transport in the porous CL and GDL of PEFCs has been a center of investigation due to the deleterious impact arising from electrochemical surface area coverage and pore blockage due to water resulting in transport limitations and performance decay in PEFCs. Pore-scale understanding of capillarity driven two-phase transport and flooding phenomena has been a central theme. Particle-based mesoscale modeling methods have been able to consider the effects of microstructure and polymer structure on water transport in Nafion and other membranes [85,101]. Dorenbos used a combined DPD - Monte Carlo modeling method to consider the effects of polymer branching on pore structure and diffusion. He was able to show that pore topology is critical to water diffusion within Nafion [101]. The DPD method was able to resolve large enough length scales to consider pore-scale diffusion; smaller scale methods such as molecular dynamics are not able to resolve large enough scales to accurately consider pore-scale effects. Addiontally, the pore-scale DPD simulations were able to identify differences in transport due to pore structure such as dead-ends and bottlenecks which are not easily described at larger or smaller length scales. Others have also investigated the effects of structure on water transport and clustering and as with Dorenbos have found that structural changes in the ionomer significantly effect water locations [85].

LBM has received significant attention in studying the effect of capillarity-wettability interactions in the PEFC CL and GDL structures. Fig. 9 shows the steady state advancing liquid water fronts inside a typical catalyst layer microstructure in response to capillary pressure increments in a primary drainage simulation, reported by Mukherjee et al. [66]. The CL microstructure used exhibits hydrophobic wetting characteristics with a static contact angle of 100°. The initially air-saturated microstructure (wetting fluid) shows larger liquid water infiltration with higher capillary pressure. The capillary fingering regime is observed at low capillary pressures whereby the liquid water saturation front exhibits finger like patterns. Surface tension driven capillary forces drive

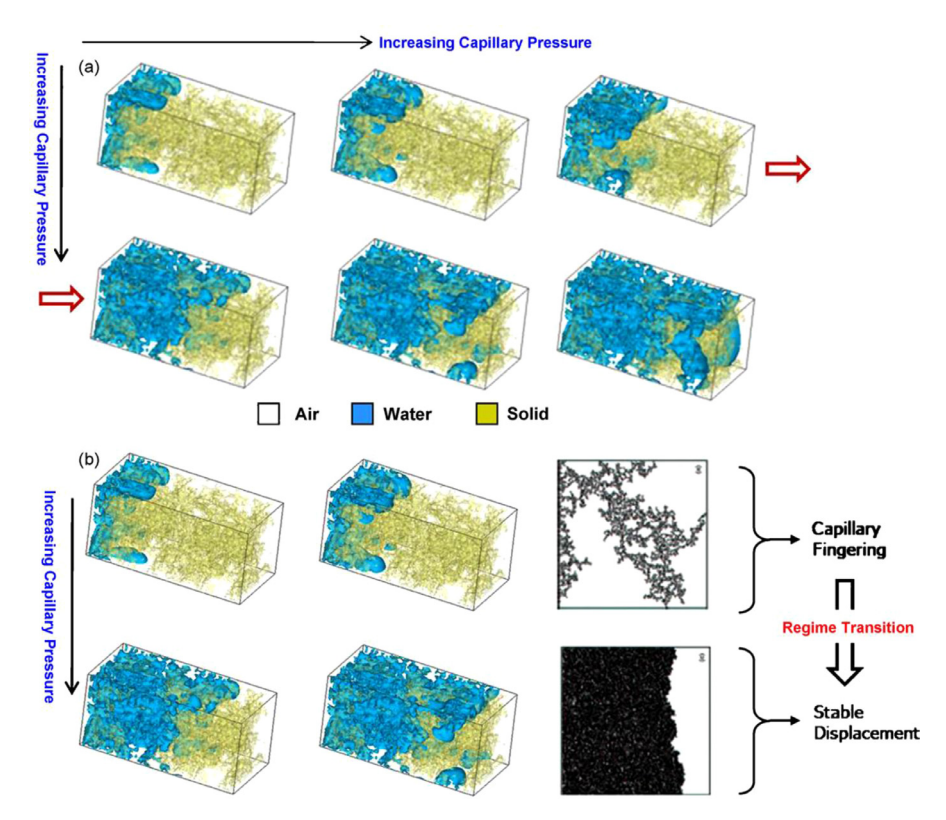


Fig. 9. Advancing liquid water front with increasing capillary pressure through the initially air-saturated reconstructed CL microstructure from the primary drainage simulation using LBM. Reprinted from [66] with permission from Elsevier.

the penetration of the liquid water phase into the resident air wetting phase region in the shape of fingers. With increasing capillary pressure, the capillary fingering regime transitions to the stable displacement regime owing to the merging of several penetrating saturation fronts. This study points to an interesting conclusion; even for extremely low capillary number flows inside the CL, the advancing liquid water front metamorphoses from a fingering structure to a somewhat flat structure as the capillary pressure rises.

Primary drainage simulations using two phase LBM are also performed by Mukherjee et al. [66] for the carbon paper GDL exhibiting higher hydrophobicity as compared to the CL investigated above, with a static contact angle of 140°. Fig. 10 displays the liquid water distribution as well as the intrusion pattern with increasing capillary pressure in the initially air saturated GDL. Owing to the stronger hydrophobicity and larger pore size, the liquid water front incursion and droplet formation ensues only at some preferential locations for low capillary pressure. As the capillary pressure increases, formation and penetration of several water fronts is observed due to capillarity. The multiple fronts coalesce and form two major chunks, which advance in the less tortuous in-plane direction. Beyond a threshold value of capillary pressure, one of the fronts reaches the air reservoir, the physical equivalent of the GDL/air interface, at a preferred location, which is termed the bubble point. These simulations reveal the strength of two-phase LBM models, which can capture intricate liquid water dynamics including droplet formation, coalescence and front propagation through the hydrophobic fibrous GDL structure.

# 3.2.5. Advantages and disadvantages

Particle methods have many advantages and disadvantages amongst themselves and when compared to mesh based modeling methods. In general, particle methods are better able to handle complex geometries and dynamic interfaces in multiphase sys-

tems. The ability to implicitly track moving interfaces without the need for dynamic and adaptive meshing increases the stability of these methods and reduces the computational cost associated with tracking boundaries. This is especially critical in mesoscale modeling of electrochemical systems where the interfaces are integral to the electrochemical reactions of the systems and are often the areas of greatest instability and performance loss, such as the issues of dendrite growth at the electrode-electrolyte interface in batteries, or the wettability of PEFC electrodes [81,82,101]. In both of those examples resolving the multiphase interfaces and multiphysics phenomena are essential to investigating those systems.

Overall particle-based methods tend to be more computationally expensive than mesh based Eulerian methods. Due to the Lagrangian nature of particle methods, neighboring particles have to be determined at every time step, which adds to the computational cost of the methods. Although with increasing computing power, wider access to high performance computing resources, and adaption to GPU computing these computational costs are becoming less of a roadblock. Additionally by coupling particle-based methods with less expensive mesh-based and statistical methods, we can develop multi-scale modeling methods that resolve the mesoscale phenomena and couple it to the large-scale system performance in a computationally efficient manner.

The DPD method has been used as a bridge to the atomic level modeling of MD. Creating a direct connection to small scale MD continues to be a challenge for continuum modeling methods. The similarities between the MD and DPD methods have allowed the direct coupling between the two methods through the interaction potentials between DPD particles, which have been parameterized based on MD simulations. Coupling to MD limits the scales DPD methods can model to the order of microsecond and nanometers but allows it to bridge the microscale to continuum level phenomena [101].

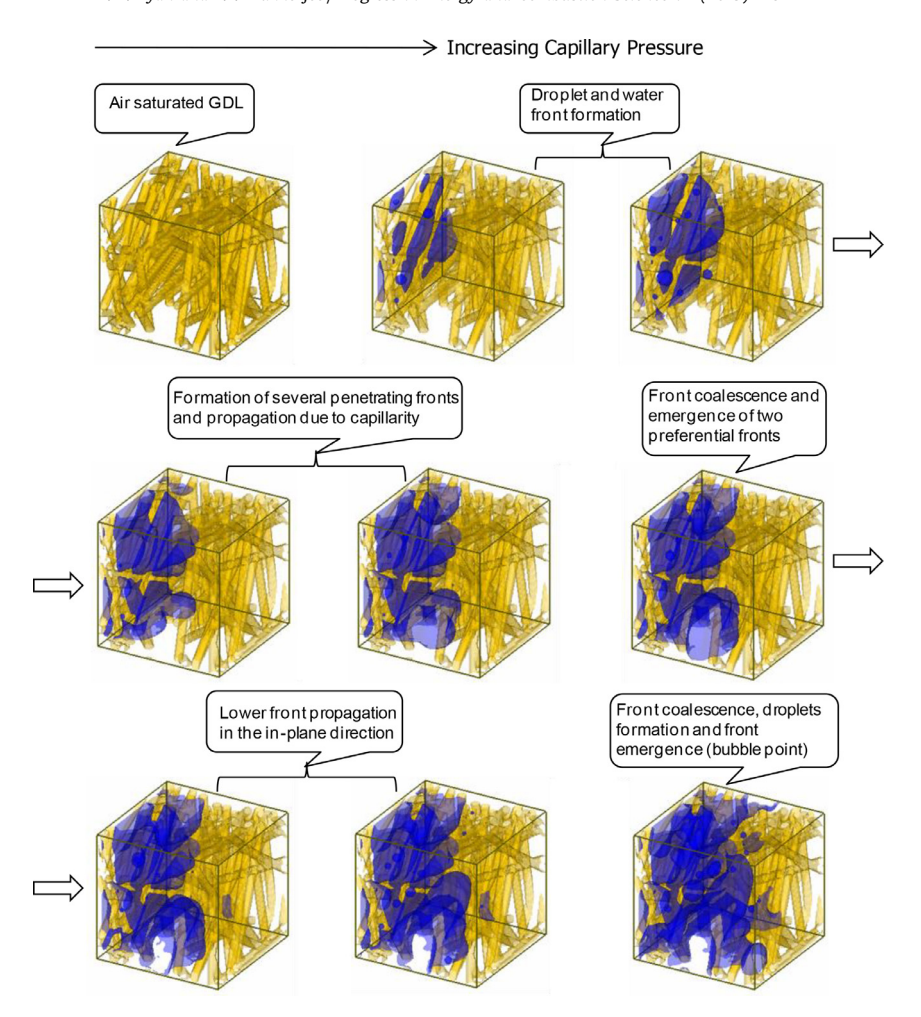


Fig. 10. Advancing liquid water front with increasing capillary pressure through the initially air-saturated reconstructed GDL microstructure from the primary drainage simulation using LBMs. Reprinted from [66] with permission from Elsevier.

Both the DPD and LBM methods require calibration of model parameters. In LBM, the primary physical parameters, such as the fluid/fluid and fluid/solid interaction parameters, need *a priori* evaluation through model calibration using numerical experiments. Similarly, DPD requires parameterization of interaction potentials via MD modeling or literature data. SPH does not require calibration of model parameters as it is based on the physical continuum governing equations (i.e. Navier-Stokes, energy conservation and species conservation). Additionally DPD is limited in that it cannot consider gas diffusion [101].

# 3.2.6. Challenges

Each of the three particle-based methods discussed in this section have challenges that need to be addressed. As with most numerical methods, there is always the drive to increase stability, consistency and convergence, and improve computational efficiency. This is true of particle-based methods and includes research into discretization of the governing equations in SPH and formulations of particle interactions in DPD. Additionally, the use of adaptive particles for multi-scale resolution is being considered to improve computational efficiency, which will allow larger, more complex systems to be considered. The implementation of boundary conditions is also an ongoing area of research and improvement in SPH and DPD. The proper formulation of boundary conditions that retain the intrinsic conservation of SPH, and properly represent the physics (i.e. no slip boundaries, inlet/outlet

conditions) has been an ongoing challenge in the SPH community [123–126].

LBM has received significant attention in modeling two-phase flow and transport in complex porous microstructures, e.g. in the PEFC CL and GDL; however it is still challenging to incorporate the full gamut of the multi-physics interactions such as species, charge and thermal transport in such electrochemical systems. A viable pathway could be to develop a hybrid approach, including LBM and CFD, which can be quite attractive in capturing the microstructure and electrochemistry coupled multi-modal transport and flow [54].

# 3.3. Fine-scale CFD

In recent years, there has been significant progress in studying electrochemistry coupled transport phenomena with microstructure resolved CFD based modeling frameworks. Conventional CFD approaches, such as the finite volume method (FVM) and finite element method (FEM), use macrohomogeneous formulations based on volume-averaged transport properties and variables over a representative elementary volume, which fail to capture the porous microstructure heterogeneity and complexity. The microscopic details of the pore structure are implicitly resolved and homogenization over the porous electrode volume is performed to obtain averaged geometric and transport properties like porosity, specific surface area, tortuosity, effective diffusivity, effective conductivity, etc. Typically, empirical correlations used to describe the

effective properties as a function of porosity and tortuosity of the porous medium are incognizant of the actual porous microstructural details, which further affect the predictive ability of such macrohomogeneous formalisms. In this regard, microstructure resolved direct numerical simulation (DNS) formalization captures the effect of microstructure-transport-electrochemistry interactions in porous structures in electrochemical energy systems. The DNS methodology also provides an effective tool for estimating effective transport property correlations representative of porous microstructures, such as constructing Bruggeman correlations.

The porous electrodes in electrochemical energy systems consist of multiple components, having distinct geometrical, physical and chemical features, enabling multifunctionality owing to electrochemistry-coupled interactions among multiple transport processes. These multi-physical interactions ultimately dictate the electrochemical properties and performance, which in turn are intricately linked to the multi-component and spatial arrangements in the porous electrode microstructures. Traditionally, porous electrode theory has been employed to understand the electrochemical response of these systems [4]. Porous electrode theory however is too restrictive in the sense that it makes quite a few assumptions regarding the structural arrangement as well as the relative length and time scales of mechanisms. Direct numerical simulation, in other words calculations performed at the pore-scale accounting for realistic geometrical features, ameliorates these shortcomings. One obvious limitation of DNS is the increased calculations, which scale in proportion to the spatial degrees of freedom. Given this dilemma, two distinct types of DNS strategies are in practice and will be discussed hereafter. The first one abstracts the real microstructural attributes based on pore-scale calculations (DNS) and this representative volume element (RVE) scale information is encoded in the porous electrode descriptions in the form of effective properties such as pore phase tortuosity and active area [65,127,128]. The other school of thought carries out all the calculations of electrochemical progressions directly at the pore-scale [129–134]. In the truest sense, the later approach is traditional DNS while the former has been termed pseudo-DNS. Both FVM and FEM based calculations can be carried out in either of these contexts. Since fundamentally electrochemical systems rely on species and charge transport, FVM calculations may be preferred owing to their inherent conservativeness. FVM and FEM are widely used in the computational field and as such are not described in detail here. The reader can find detailed descriptions of the theory and formulation of FVM and FEM in the literature [135,136].

# 3.3.1. DNS fundamentals: effective property estimation

Porous microstructures are typically characterized in terms of their effective properties to offer insights into relevant transport and interfacial interactions. These effective properties essentially account for the spatial arrangement of different phases and how they lead to quantitatively different behaviors compared to the bulk phase. For example, ionic transport in the bulk electrolyte is characterized by ionic conductivity and diffusivity, but when the electrolyte is filled in a complicated pore network, this transport is further affected by geometrical features such as pore size, shape and connectivity. The effect of these attributes is quantified in terms of properties such as porosity and tortuosity. Once reconstructed electrode volumes are available, DNS calculations are performed to assess these properties. Porosity is computed by integrating over the pore phase volume, while the interfacial area is estimated via summing over phase boundaries. Calculation of other properties such as tortuosity is more intensive. Consider species transport [65] in a complex pore network filled with electrolyte. The steady state concentration profile in the bulk is dictated by the elliptic equation:

$$\nabla \cdot (D\nabla C) = 0 \tag{52}$$

where *D* is diffusivity in the bulk electrolyte. In a porous electrode structure, this species transport will not take place in locations that contain solid phase(s). When this species transport is averaged over an RVE, the above governing equation transforms to:

$$\nabla \cdot \left( D^{eff} \nabla \tilde{C} \right) = 0 \tag{53}$$

where  $D^{eff}$  is effective diffusivity and  $\tilde{C}$  represents the concentration field in an RVE. For liquid electrolytes, diffusion is isotropic in the bulk (i.e., no directional dependence) when volume averaged over a porous electrode, it becomes a tensor since tortuosities in each of the coordinate directions can be different. In other words,  $D_X^{eff} = D \varepsilon / \tau_X$  where  $\varepsilon$  is open porosity and  $\tau_X$  is tortuosity in that particular direction. In order to obtain a tortuosity value in a particular direction, say x, concentrations are fixed at the two ends (C=1 at x=0 and C=0 at  $x=L_X$  planes) and the other four surfaces  $(y=0,L_y)$  and  $z=0,L_z)$  have zero flux across them. Once the corresponding pore-scale concentration field is available, species flux is computed in the direction of interest (since steady state profiles are sought,  $I_X = \text{constant}$  at any x):

$$J_{x} = \int_{x=x \text{ plane}} -D \frac{\partial C}{\partial x} dy dz$$
 (54)

At the RVE scale,

$$J_{x} = -D_{x}^{eff} \frac{\partial \tilde{C}}{\partial x} = -D_{x}^{eff} \left( \frac{C_{x=L_{x}} - C_{x=0}}{L_{x}} \right)$$
 (55)

Equating the two and using the relation  $D_x^{eff} = D\varepsilon/\tau_x$ , one back computes pore network tortuosity in the given coordinate direction. A similar procedure is repeated to get the other two tortuosities:  $\tau_y$  and  $\tau_z$ . For a sample LIB composite electrode, the steady state concentration profile in the pore phase is shown in Fig. 11 for the three coordinate directions.

Typically, in electrodes, the pore phase facilitates ionic transport, while the solid phase is responsible for electronic conduction. The conductivity calculations are carried out in a similar fashion as the tortuosity. One additional consideration is to ensure the continuity of electron flow at an interface of the two adjoining solid phases. Like the concentration equation (Eq. (52)) for tortuosity, the electric potential equation is solved for conductivity estimation. Representative electric potential contours are given in Fig. 11 as well.

The DNS approach has proven to be a viable method for estimating effective transport properties, such as oxygen diffusivity, electronic and ionic conductivity in the CL, GDL and ML of a PEFC. Fig. 12 shows the DNS-based numerical estimation along with experimental measurement of the effective oxygen diffusivity and electron conductivity of a typical PEFC nonwoven carbon paper GDL, reconstructed from XCT imaging, under different compression pressures which affect the underlying microstructure and hence the effective properties [137]. This study highlights the efficacy of the DNS approach in estimating the influence of porous microstructures on the effective transport properties for electrochemical energy systems.

It is important to recognize the correlation between the evolution of predictive modeling and its intended application. Porous electrodes (electrochemical reactors) were proposed five decades ago with the goal to increase the reaction surface area per unit volume. This comes at the cost of pore-scale transport resistance. The porous electrode theory was thus proposed to understand the complexations arising from the porous three-dimensional nature of the reacting medium without having to carry out calculations at the pore-scale [138]. At this stage, neither the accurate 3D structural information (e.g., imaging) nor the accurate modeling and computational framework were available to study precise three-dimensionality, and the porous electrode theory pro-

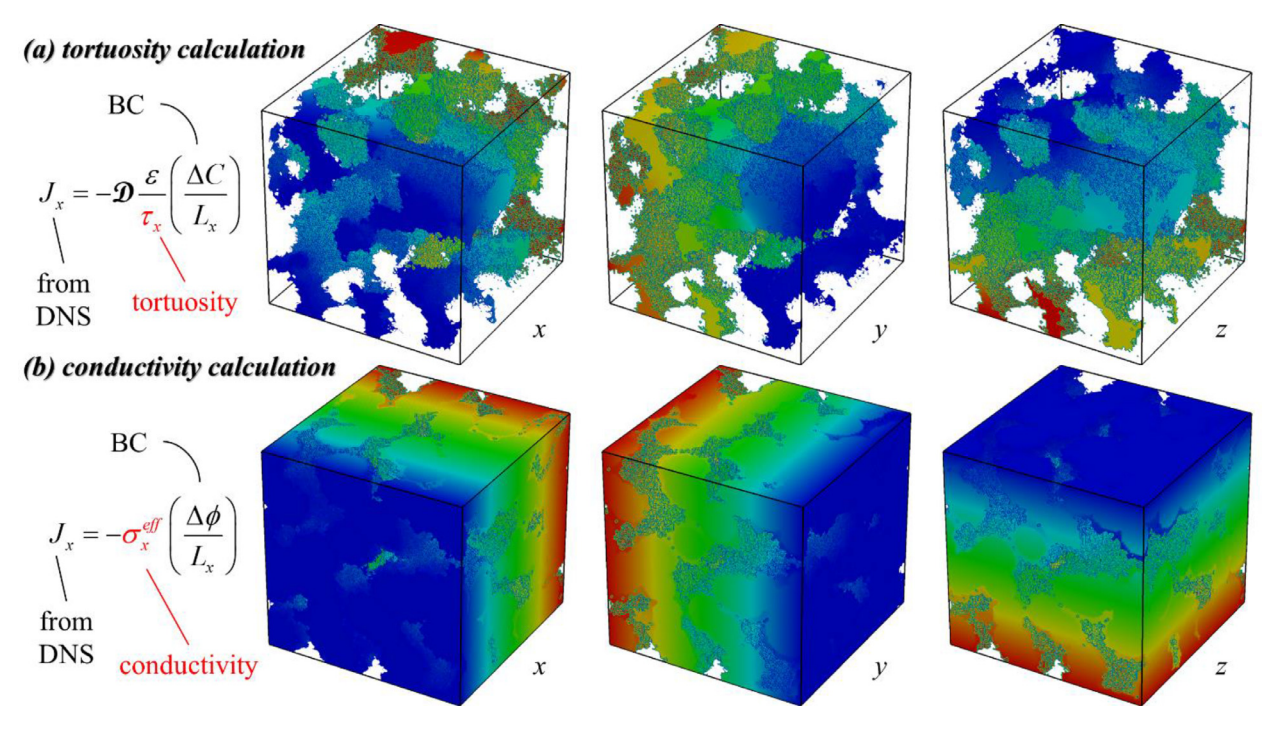


Fig. 11. Effective property calculations. (a) Steady-state concentration fields for pore phase tortuosity calculations in three coordinate directions. (b) Steady-state potential fields for effective conductivity calculations in the solid phase. Reprinted with permission from [65]. Copyright 2018 American Chemical Society.

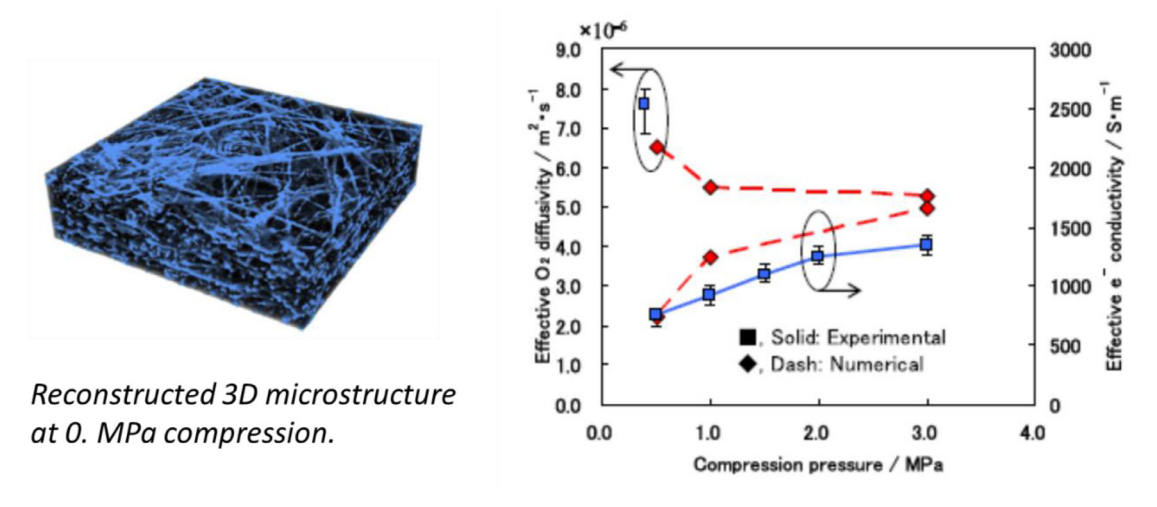
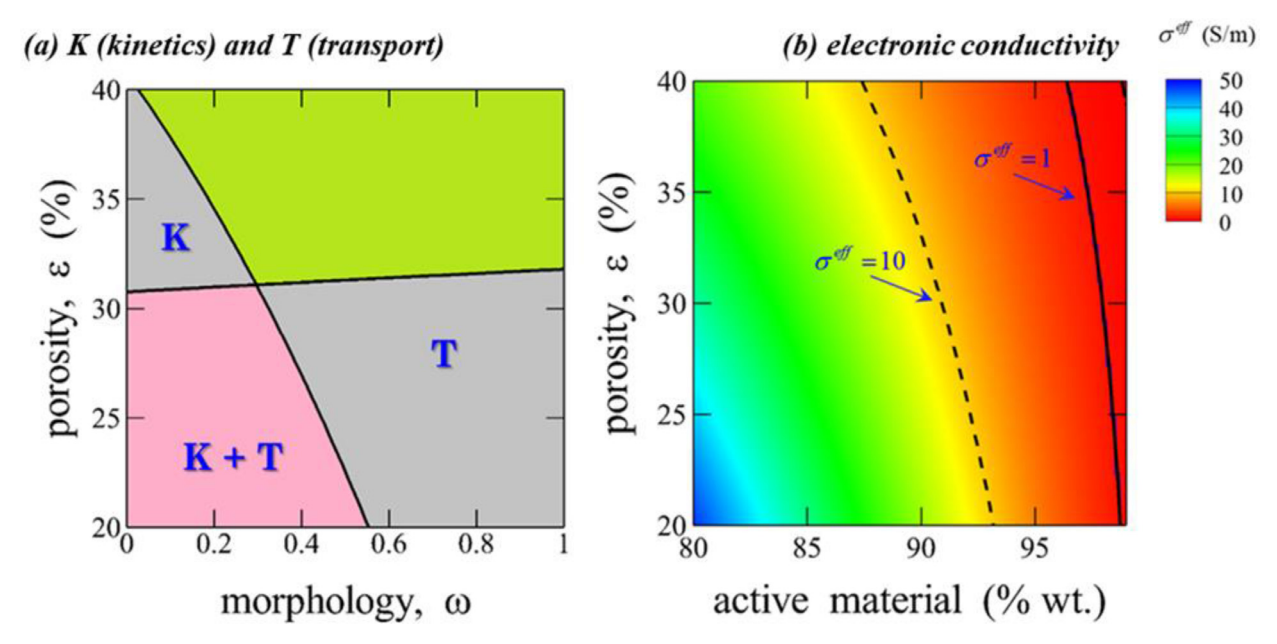


Fig. 12. Effective property (oxygen diffusivity and electron conductivity) estimation of a fibrous GDL in a PEFC. Reprinted from [137] with permission from Elsevier.

vided a reasonable understanding of these effects [139] (at best the quantitative scales). With the new material discovery in recent years, the electrode structures have become more complicated [140,141], and require commensurate advances in the mathematical treatment of porous electrodes. DNS based effective property calculations [142,143] have quite suitably accounted for such microstructural realism with minimalist computational overhead for electrode-scale electrochemical interactions [65,128,144]. Such an approach has also fostered the study of evolving electrochemical systems such as lithium-sulfur batteries which undergo considerable microstructural changes during their operation [145,146]. Such a pseudo-DNS approach allows one to consistently deconvolute the representative pore-scale effects and how they scale at larger electrode thickness length-scales [147]. Electrode-scale DNS would not elucidate such an intricate scale-bridging interplay. The next generation energy storage systems are much more complicated, partly due to their severe geometrical changes, for example, high volume expansion materials such as silicon [148] and tin [149], lithium foil [150] and similar metallic film electrodes and porous hosts [151]. The associated complexities would make electrode-scale DNS calculations essential to the physicochemical interpretation of such systems. Additionally, the extreme response of present-day technologies such as fuel cell corrosion, repeated cycling or extreme fast charging of lithium-ion cells, also demands DNS computations to access physical insights into these systems (e.g., Fig. 16). A judicious selection from this spectrum of DNS strategies is invariably a compromise between the level of details and the particular phenomenon being studied.

# 3.3.2. Notable results

Here we present representative highlights of DNS modeling with a focus on electrode microstructural complexations and how these give rise to the thermo-electrochemical attributes related to performance and safety aspects of electrochemical systems. As



**Fig. 13.** The secondary phase introduces nonlinear effects on RVE scale transport processes. It increases the kinetic and electrolyte transport resistance, and it also increases the effective electronic conductivity. The morphology of these secondary solids is also quite relevant since it dictates the relative importance of short- and long-range interactions. (a) RVE scale resistance for a composite electrode with 95% wt. active material. (b) Effective electronic conductivities as a function of electrode composition. Secondary phase = 100% – active material. Reprinted with permission from [65]. Copyright 2018 American Chemical Society.

alluded to earlier, the composite electrodes in LIBs contain nonintercalating solids: conductive additives for electronic conductivity (typically the Li storing phase on the cathode side has very low electronic conductivity) and polymeric binder to ascribe mechanical stability. However, on the flip side, the presence of these secondary solids limits the space available for ionic transport (i.e., electrolyte) as well as Li storage (i.e., active material), and in turn reduces the specific energy and power. Additionally, these secondary phases alter the pore network and partially cover the active material surface area. In other words, the presence of a secondary phase increases the pore phase transport resistance and kinetic resistance to intercalation due to reduced electrochemically active area. These complexations are plotted in Fig. 13 based on the effective property characterization results via pseudo-DNS for such composite cathodes. These microstructural interactions permeate to the electrochemical response of the corresponding electrodes, and are discussed elsewhere [65,127].

Since the relevant charge transport and conversion take place at the pore-scale, heat generation is always accompanied given the finite rate of these processes. Additionally, entropy change during operation also manifests as heat. Fig. 14 schematically identifies these distinct contributions, where representative composite electrode structures are shown along with the color legends for different material phases. Reduced porosity and/or increased tortuosity leads to greater Joule heating due to increased ionic transport resistance. On the other hand, if porosity is increased (at identical active material to secondary phase composition by weight), electronic conductivity reduces which increases the Joule heating due to the electronic conduction limitation. Different phase arrangements as well as their contents alter the electrochemically active area, which correlates to the kinetic overpotential, and equivalently the heat generation related to charge transfer resistance. Note that reduced porosity means the electrode can house more electrochemical energy, but at the cost of higher intrinsic heat generation

This intricate relation of porosity, electrochemical operation and temperature rise due to heat generation is explored in Fig. 15. First consider figures (c) and (d) which detail cell capacity when oper-

ated at different rates (at different ambient temperatures). As the porosity is decreased, achievable capacity increases since more active material is present in the same volume. When the porosity is around a lower threshold, the ionic resistance can shutdown the electrochemical electrodes. In this regime, the capacity drops drastically. The onset of this ionically induced shutdown is earlier as the operation is carried out at a higher current. Next consider the corresponding thermal interactions (subfigures (a) and (b)). As porosity is reduced, temperature rises to greater values, which pushes the cell from safe to risk or risk to unsafe limits. At too low porosities, since the electrochemical operation is terminated early, not enough heat is generated to increase the temperature to concerning levels. The severity again is exacerbated if the operation is carried out at a higher ambient temperature. In this event, efficiency of convective cooling decreases and in turn zones for unsafe and potential risk operation expand. These calculations highlight a critical limit of LIB technology from a thermal safety standpoint: high energy cells have severe thermal experiences.

Previous illustrations detail the pseudo-DNS approach where all the essential phases and microstructural features are characterized and passed on to the porous electrode theory based electrochemical description. On the other hand, in a typical DNS approach, electrochemistry coupled species and charge transport processes are solved directly on a small enough RVE of the porous electrode microstructure. Mukherjee and Wang [152,153] were the first to present such a DNS approach to study the electrochemical reaction kinetics, species and charge transport to characterize the physical processes occurring inside the porous cathode CL of a PEFC. This DNS method was based on a single-domain FVM framework, which included charge transfer kinetics of the oxygen reduction reaction occurring at the electrochemically active sites characterized by the triple phase boundary, oxygen and water vapor transport though the pore phase, and proton (charge carrier) transport in the electrolyte phase. This approach enabled studying the compositional influence on the PEFC CL performance as well as local overpotential and reaction current distributions. Following this DNS approach, several studies by other groups appeared in the literature [64,154–157]. As a representative example, the DNS model

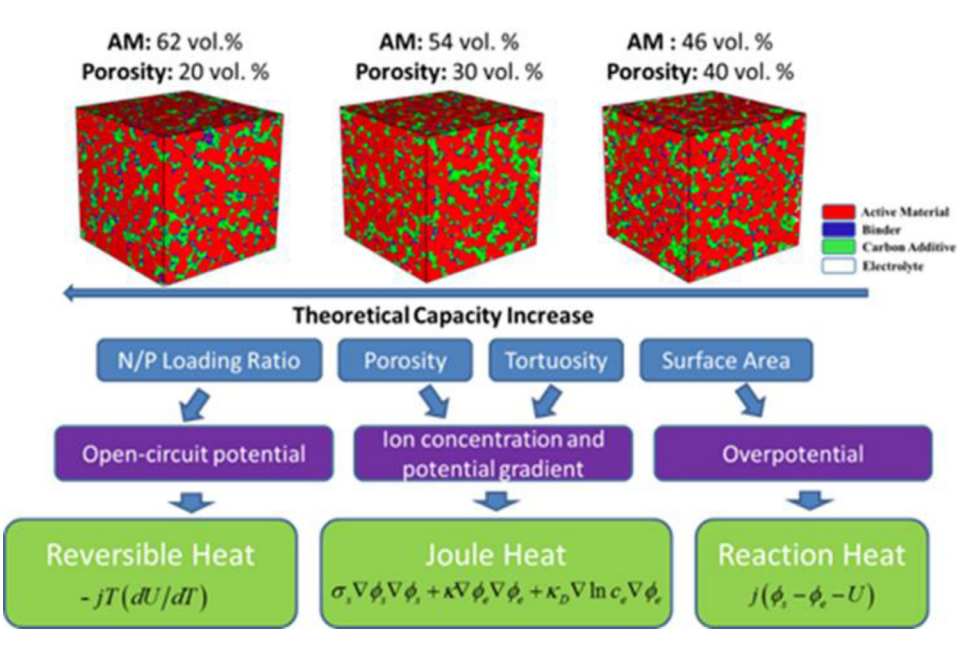


Fig. 14. Pore-scale origins of heat generation during electrochemical functioning of an intercalation electrode for different porosities and active material (AM) loading. Reproduced from [128] with permission from the Journal of the Electrochemical Society. Copyright 2017, The Electrochemical Society.

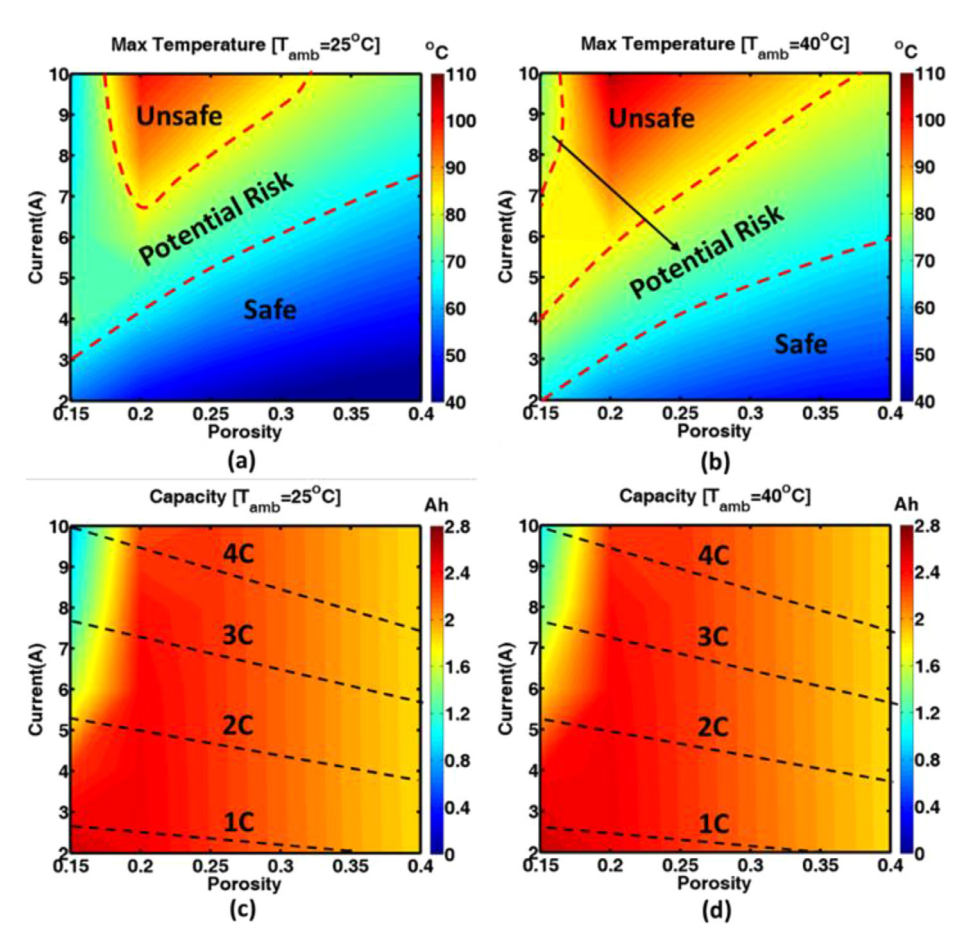


Fig. 15. Microstructure affects electrochemistry and thermal interactions. The severity of thermal interactions is assessed in the form of maximum temperature rise, while electrochemical response is quantified from achievable capacity. Reproduced from [128] with permission from the Journal of the Electrochemical Society. Copyright 2017, The Electrochemical Society.

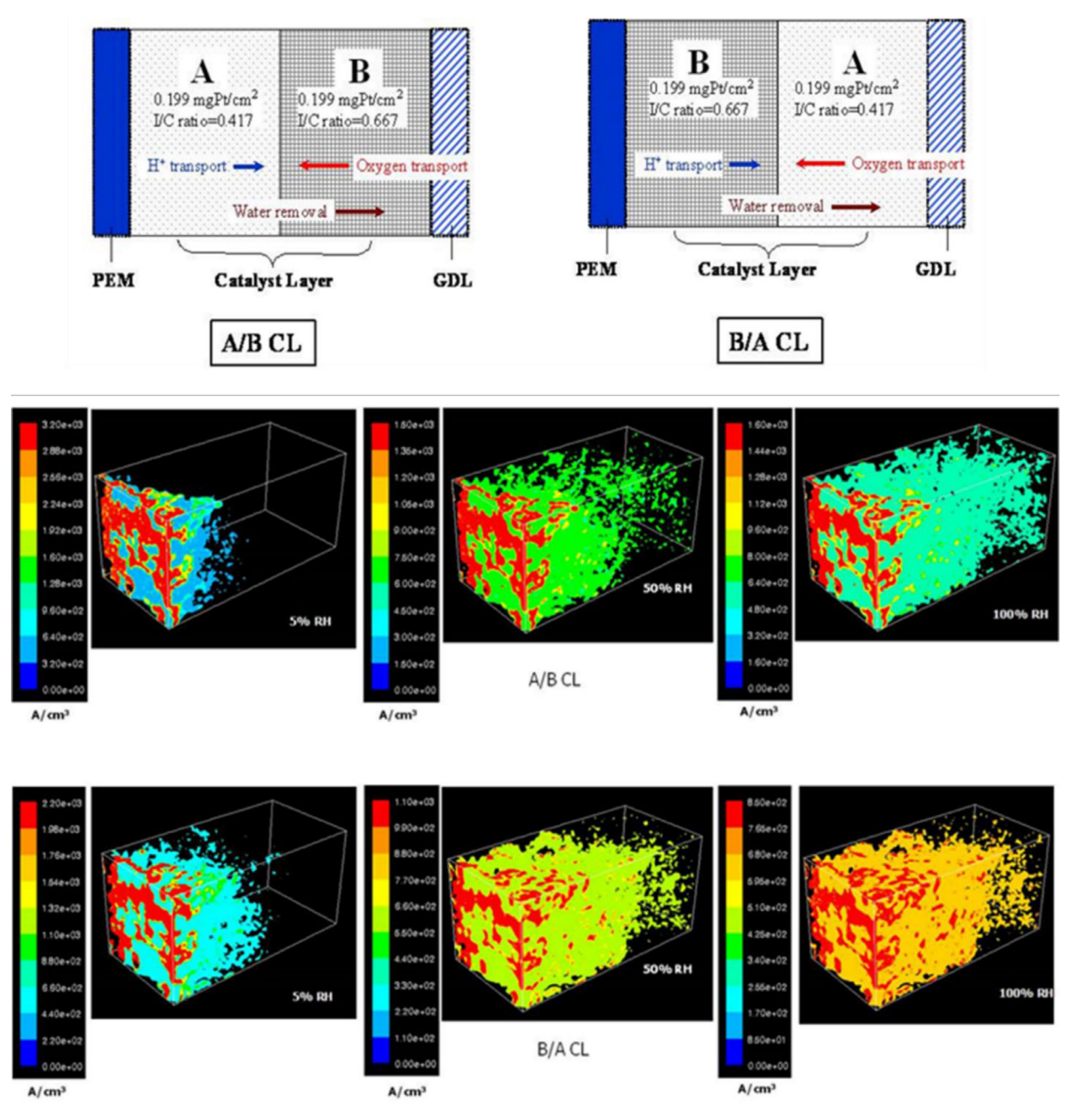


Fig. 16. 3-D reaction current distribution contours in two bi-layer CLs, with opposing gradients in pore and electrolyte phase volume fractions as schematically represented, at different relative humidity operating conditions for a typical PEFC based on the DNS calculations. Reproduced from [153] with permission from the Journal of the Electrochemical Society. Copyright 2007, The Electrochemical Society.

was used to study the influence of structural variation of a bi-layer cathode CL in a PEFC on the underlying transport and performance [153]. The design of the bilayer CL incorporates physical collocation of two catalyst-coated membrane layers, designated as A and B layers, each with equal platinum catalyst loading and thickness. The two layers differ in the ionomer to carbon (I/C) weight ratios, which leads to varying pore and electrolyte phase volume fractions. Fig. 16 displays the 3-D reaction current distributions for different relative humidity conditions, which affect the underlying proton and oxygen transport, and electrochemical reactions. It is evident that a high humidity operation results in higher reaction current density distribution, thereby minimizing the overpotential loss and enhancing CL utilization. The lower relative humidity conditions exhibit reaction current snap off which renders a signifi-

cant portion of the CL, with the expensive platinum catalyst, virtually inactive. This study highlights that a suboptimal porosity near the CL /GDL interface compounded by the reaction zone shift towards membrane-CL interface in the A/B CL inhibit oxygen transport resulting in inferior performance as compared to the B/A CL. The results further emphasize the importance of the DNS models in elucidating a detailed pore-scale description of the underlying transport in the PEFC CL microstructure and other electrochemical electrode designs.

A similar DNS modeling strategy was later employed to study electrochemical and species/charge transport characteristics in the LIB electrode RVEs as well. Fig. 17 shows an example of the lithiation dynamics of a Nickel Cobalt Aluminum Oxide electrode [129]. Four distinct electrode structures are extracted to investigate the

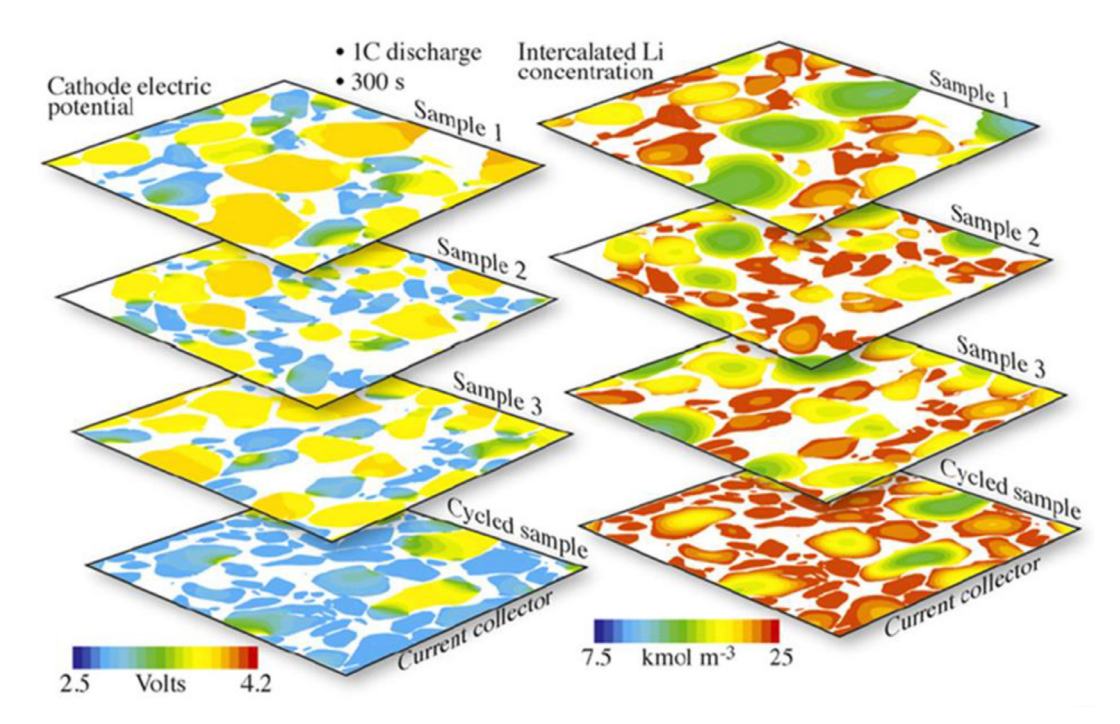


Fig. 17. Pore-scale electrochemical study of electrode operation. Four different electrodes are imaged via FIB-SEM and their intercalation dynamics is studied revealing microstructural dependence. Reproduced from [129] with permission of Elsevier.

dependence of electrochemistry on structural arrangement. The study reveals that the distribution of the solid phase potential closely correlates with the instantaneous state of lithiation and particle dimensions. Smaller particles undergo more uniform lithiation and subsequently the state of charge is higher (equivalently smaller potential) when analyzed at a fixed instant of time after lithiation. It is important to note that DNS modeling of LIB electrodes has received significant recent attention [63,158–160].

# 3.3.3. Advantages and disadvantages

The DNS approach is well positioned to take advantage of the tremendous progress in CFD based simulation methods with high-fidelity computational schemes and advanced software platforms. The multi-physics coupling inherent in porous electrodes for electrochemical energy systems can be captured with relative sophistication. However, a critical aspect in such simulations is the inherent importance of the interface driven electrochemically reactive processes, which rely heavily on the resolution of the triple phase and/or pore/solid boundaries. Since the DNS method is a grid-based fine-scale CFD approach, the interface resolution requires grid generation complexity, which may escalate the computational cost. A voxel-based approach on the other hand can reduce the grid generation complexity as well as computational cost, however it suffers from adequate representation of the inherently complex interfaces. As compared to the particle-based approaches, the DNS method is more flexible and adaptable to incorporating different physics-based processes through appropriate governing differential equation constructs and relative ease of the boundary condition implementation.

# 3.3.4. Challenges

The fine-scale CFD based DNS approach has witnessed a steadily growing interest in recent years to study reactive-diffusion processes in porous electrodes. However, this approach is fraught with some challenges. Resolving the interface in complicated porous electrode microstructures is critical due to the very nature of the interface driven electrochemically reactive processes coupled with species and charge transport. This would require

advances in sophisticated workflow including experimental image processing (e.g. XCT data), microstructure reconstruction and interface capturing techniques in order to consider a reasonable size of the electrode microstructure domain for high-fidelity assessment of the influence of heterogeneities on the electrochemical and transport properties and performance. Another challenge is how to capture interface evolution due to a side reaction, for example formation of the solid electrolyte interphase or lithium electrodeposition in LIBs. The DNS approach would require significantly novel ways to handle such phenomena. Although the fine-scale CFD method is quite effective for modeling reactivediffusive processes in porous microstructures, studying two-phase flow consisting of the capillarity-wettability-interface interaction, such as in the case of PEFCs, is challenging. Undoubtedly, the DNS method is a powerful mesoscale technique; however, there is plenty of room for fundamental advancements in both numerical and physics-based sophistications that can push the envelope for microstructure-transport-reaction interactions in electrochemical energy systems.

#### 4. Summary

As discussed in this review there are several computational methods being developed for the simulation of electrochemical devices and each method has unique advantages and disadvantages that make it well suited for different applications. The particle-based methods such as LBM, SPH, and DPD, are well suited for modeling complex and deforming geometries; while DNS takes advantage of the computational and algorithmic advances of the mature CFD field and is easily able to incorporate the complex physics and boundary conditions of the electrodes.

Mesoscale modeling has been used to investigate the design, performance, and fundamental physics of SOFCs, PEFCs, and LIBs. These studies have provided valuable insights into how mesoscale phenomena affects the macro-scale behavior of electrochemical devices, such as microstructural effects on water transport in PEFCs, or dendrite growth in lithium batteries.

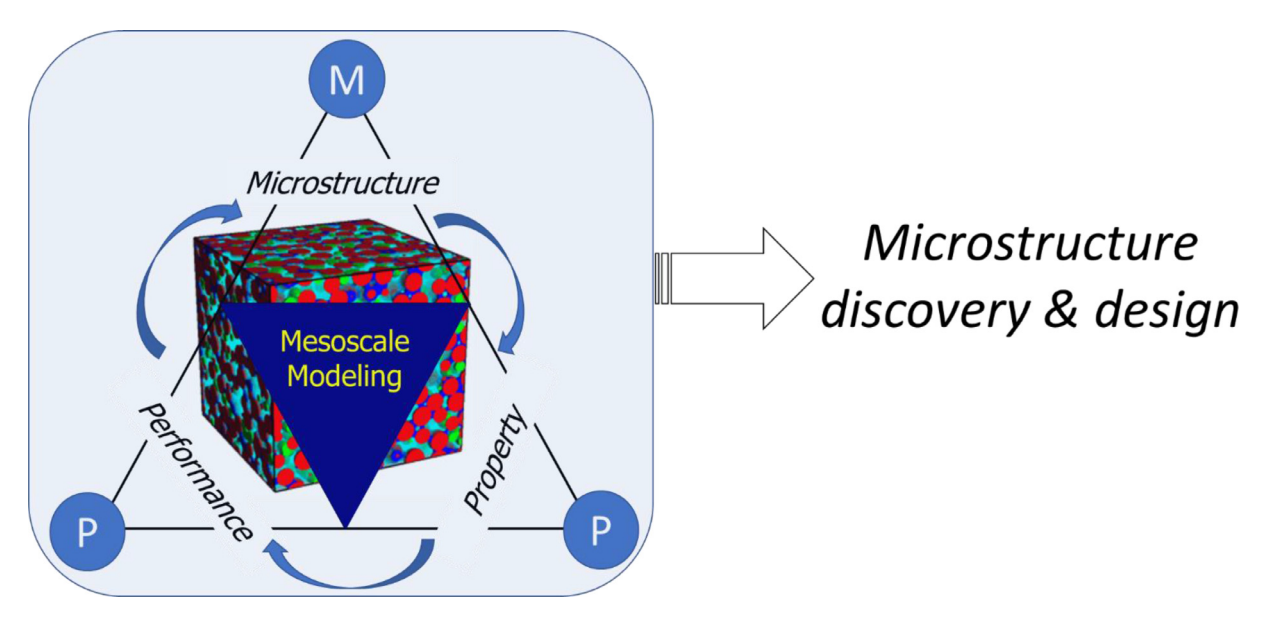


Fig. 18. Mesoscale modeling paradigm and perspective.

Continued advances in the numerical methods and computational resources will allow mesoscale modeling to play a more prominent role in the research and development of advanced electrochemical energy systems. Additionally they will be critical in advancing use of rational materials design for electrochemical devices and for the development of multi-scale modeling methods.

#### 5. Challenges and future perspective

Understanding the mesoscale interactions is critical to the improvement in performance, safety and life of electrochemical energy systems. Mesoscale modeling is poised to play an exceedingly important role in discerning the microstructure complexations of electrochemistry coupled transport phenomena that directly affect the system response, Fig. 18. Such a mesoscale paradigm can serve as a bridge between materials discovery and system response. Hence, there is a crucial need for advancing the mesoscale modeling predictions to inform microstructure discovery and design.

There are several challenges facing the further development of these computational methods. The most significant of those is the lack of experimental data for the verification and validation of the models and for input parameters for the models. It is very difficult, if not impossible, for current experimental methods to resolve mesoscale phenomena in situ. The macro-scale data that is available is difficult to relate back to the mesoscale physics and requires assumptions and extrapolation of data for comparison to mesoscale models. Concurrent development of advanced experimental characterization and visualization techniques are needed to allow the realization of the full power and potential of mesoscale modeling methods in advancing the architecture design and discovery in electrochemical energy systems.

As advances in experimental and computational methods continue there are vast areas where mesoscale modeling could be a significant asset to the electrochemical field. Rationale design of materials systems is one such area. Starting with the Materials Genome Initiative [161], there has been a significant push in recent years to take advantage of the vast computational resources to accelerate the development of new materials. Electrochemical energy systems is one field that is ripe to take advantage of this. Molecular scale modeling and high throughput computing have been applied to areas such as new electrolyte or electrode materials discovery in LIBs. However, as several of the studies highlighted in this re-

view point out for most electrochemical devices the critical design aspects are not just the materials used but also the mesoscale architecture of the materials, such as the porous electrodes. To truly advance their designs both the materials and the microstructure must be considered and mesoscale modeling can bridge this gap.

Another critical area where mesoscale modeling can help advance electrochemical systems is in the safety of these devices. This is especially critical for the advancement of lithium batteries. The thermal response of LIBs under abuse conditions such as short-circuiting, overcharging, thermal runaway, and mechanical failure are critical research areas for the improvement of current LIB technologies and for the advancement of lithium metal batteries [162]. As discussed in the DNS section mesoscale modeling has shown that the electrodes can experience local extreme temperature conditions. At this point most research into safety issues has focused on experimental testing and characterization. Most computational efforts in this area have considered simplified one dimensional models, and hybrid, multidimensional models [162–164]. However, few modeling efforts have considered safety issues at the mesoscale, which could help in understanding thermal responses to abuse conditions. Current mesoscale modeling efforts into dendrite growth could be used a starting point for expansion into safety modeling by addition of thermal models in the presence of dendrites.

The use of mesoscale modeling in materials system design raises the second major challenge for these computational methods, namely the computational cost of running simulations. By their nature, mesoscale models are computationally expensive as they resolve the detailed microstructures and multi-physics interactions. However, with the continuing advances in computational power and expanding high performance computing resources this challenge is not a major roadblock to the continued and expanded use of mesoscale methods. Additionally, mesoscale methods are being developed for use in multi-scale modeling approaches where a limited number of expensive mesoscale simulations can be used to inform more efficient upscaled and statistical based models [87,101,116,118].

#### **Acknowledgements**

PPM acknowledges financial support in part from the U.S. Department of Energy CAEBAT III program, and NSF grant no.

1438431/1759651. PPM also acknowledges Aashutosh Mistry and Ankit Verma, Ph.D. candidates working with him at Purdue University, for their assistance with this manuscript preparation. EMR acknowledges financial support in part from NSF grant no. 1727316.

#### References

- Schmidt L. The engineering of chemical reactions. New York: Oxford University Press: 1998.
- [2] Oldham KB, Myland JC. Fundamentals of electrochemical science. San Diego: Academic Press, Inc.; 1994.
- [3] Bessler WG, Gewies S, Vogler M. A new framework for physically based modeling of solid oxide fuel cells. Electrochim Acta 2007;53:1782–800.
- [4] Newman J, Thomas-Alyea KE. *Electrochemical systems*. John Wiley & Sons, Inc.; 2012
- [5] Adams DM, Brus L, Chidsey CED, Creager S, Creutz C, Kagan CR, et al. Charge transfer on the nanoscale: current status. J Phys Chem B Mater 2003:107:6668–97.
- [6] Zeng Y, Bai P, Smith RB, Bazant MZ. Simple formula for asymmetric Marcus-Hush kinetics. J Electroanal Chem 2015;748:52–7. doi:10.1016/J.JELECHEM. 2015.04.018.
- [7] Zeng Y, Smith RB, Bai P, Bazant MZ. Simple formula for Marcus-Hush-Chidsey kinetics. J Electroanal Chem 2014;735:77-83. doi:10.1016/J.JELECHEM.2014.09.
- [8] Bai P, Bazant MZ. Charge transfer kinetics at the solid-solid interface in porous electrodes. *Nat Commun* 2014:5:3585.
- [9] Singhal S, Kendall K. High temperature solid oxide fuel cells. Oxford: Elsevier; 2006.
- [10] O'Hayre R, Cha S-W, Colella W, Prinz F. Fuel cell fundamentals. New York: John Wily and Sons; 2006.
- [11] Ryan EM, Khaleel MA. Modeling solid oxide fuel cells from the macroscale to the nanoscale. Fuel Cell Sci. Eng., Wiley-VCH Verlag GmbH & Co. KGaA; 2012. p. 733-66. doi:10.1002/9783527650248.ch26.
- [12] Zhu H, Kee RJ. Modeling distributed charge-transfer processes in SOFC membrane electrode assemblies. J Electrochem Soc 2008;155:B715-29.
- [13] Incropera FP, DeWitt DP. Fundamentals of heat and mass transfer. 5th ed. New York: John Wiley and Sons; 2002.
- [14] Resch E, Pharoah J. Numerical and experimental characterisation of convective transport in solid oxide fuel cells. Queen's University; 2008.
- [15] Santamaria AD, Cooper NJ, Becton MK, Park JW. Effect of channel length on interdigitated flow-field PEMFC performance: a computational and experimental study. Int J Hydrogen Energy 2013;38:16253-63. https://doi.org/10. 1016/j.ijhydene.2013.09.081.
- [16] Cussler EL. Diffusion: mass transfer in fluid systems. Cambridge: Cambridge University Press; 1997. p. 177–8.
- [17] Arnost D, Schneider P. Dynamic transport of multicomponent mixtures of gases in porous solids. Chem Eng J Biochem Eng J 1995;57:91-9.
- [18] Bird B, Stewart W, Lightfoot E. Transport phenomena. Second. New York: John Wiley & Sons, Inc.; 2002.
- [19] Mason EA, Malinauskas AP. Gas transport in porous media: the dusty-gas model. Amsterdam: Elsevier; 1983.
- [20] Coppens MO, Froment GF. Knudsen diffusion in porous catalysts with a fractal internal surface., vol. 3. Curacao, Dutch Antilles: World Scientific; 1995. p. 807–20.
- [21] Jeon DH, Kim H. Effect of compression on water transport in gas diffusion layer of polymer electrolyte membrane fuel cell using lattice Boltzmann method. J Power Sources 2015;294:393–405. doi:10.1016/j.jpowsour.2015.06. 080.
- [22] Xiao J, Mei D, Li X, Xu W, Wang D, Graff GL, et al. Hierarchically porous graphene as a lithium-air battery electrode. *Nano Lett* 2011; 11:5071-8. doi:10. 1021/nl203332e.
- [23] Kitaura H, Zhou H. Electrochemical performance and reaction mechanism of all-solid-state lithium-air batteries composed of lithium, Li1+xAlyGe2-y(PO4)3 solid electrolyte and carbon nanotube air electrode. Energy Environ Sci 2012;5:9077–84.
- [24] Antcak G, Ehrlich G. The beginnings of surface diffusion studies. *Surf Sci* 2005;**589**:52–66.
- [25] Shi Y, Cai N, Li C. Numerical modeling of an anode-supported SOFC button cell considering anodic surface diffusion. J Power Sources 2007;164:639–48.
- [26] Williford RE, Chick LA. Surface diffusion and concentration polarization on oxide-supported metal electrocatalyst particles. Surf Sci 2003;547:421–37.
- [27] Bandhauer TM, Garimella S, Fuller TF. A critical review of thermal issues in lithium-ion batteries. J Electrochem Soc 2011;158:R1–25.
- [28] Wang C-Y. Fundamental models for fuel cell engineering. *Chem Rev* 2004;**104**:4727–66. doi:10.1021/cr020718s.
- [29] Weber AZ, Newman J. Modeling transport in polymer-electrolyte fuel cells. Chem Rev 2004;104:4679–726. doi:10.1021/cr020729l.
- [30] Mukherjee PP, Pannala S, Turner JA. Modeling and simulation of battery systems. In: Daniel C, Besenhard JO, editors. *Handb. Batter. Mater.*. WILEY-VCH Verlag; 2011. p. 843–75.
- [31] Pals CR, Newman J. Thermal modeling of the lithium/polymer battery. J Electrochem Soc 1995;142:3282-7.

- [32] Wang CY, Srinivasan V. Computational battery dynamics (CBD) electrochemical/thermal coupled modeling and multi-scale modeling. J Power Sources 2002;110:364–76. doi:10.1016/S0378-7753(02)00199-4.
- [33] Bernardi D, Pawlikowski E, Newman J. A general energy balance for battery systems. J Electrochem Soc 1985;132:5–12. doi:10.1149/1.2113792.
- [34] Cocco AP, Nelson GJ, Harris WM, Nakajo A, Myles TD, Kiss AM, et al. Three-dimensional microstructural imaging methods for energy materials. *Phys Chem Chem Phys* 2013;15:16377–407. doi:10.1039/C3CP52356J.
- [35] Chen-Wiegart YCK, Liu Z, Faber KT, Barnett SA, Wang J. 3D analysis of a LiCoO2-Li(Ni1/3Mn 1/3Co1/3)O2 Li-ion battery positive electrode using xray nano-tomography. Electrochem Commun 2013;28:127–30. doi:10.1016/j. elecom.2012.12.021.
- [36] Chen-Wiegart YK, Shearing P, Yuan Q, Tkachuk A, Wang J. 3D morphological evolution of Li-ion battery negative electrode LiVO2 during oxidation using X-ray nano-tomography. Electrochem Commun 2012;21:58–61. https://doi.org/ 10.1016/j.elecom.2012.04.033.
- [37] Sun F, Osenberg M, Dong K, Zhou D, Hilger A, Jafta CJ, et al. Correlating morphological evolution of Li electrodes with degrading electrochemical performance of Li/LiCoO2 and Li/S battery systems: investigated by synchrotron X-ray phase contrast tomography. ACS Energy Lett 2018;3:356–65. doi:10.1021/acsenergylett.7b01254.
- [38] Finegan DP, Scheel M, Robinson JB, Tjaden B, Hunt I, Mason TJ, et al. In-operando high-speed tomography of lithium-ion batteries during thermal runaway. *Nat Commun* 2015:**6**:6924.
- [39] Taiwo OO, Finegan DP, Paz-Garcia JM, Eastwood DS, Bodey AJ, Rau C, et al. Investigating the evolving microstructure of lithium metal electrodes in 3D using X-ray computed tomography. Phys Chem Chem Phys 2017;19:22111–20. doi:10.1039/C7CP02872E.
- [40] Taiwo OO, Loveridge M, Beattie SD, Finegan DP, Bhagat R, Brett DJL, et al. Investigation of cycling-induced microstructural degradation in silicon-based electrodes in lithium-ion batteries using X-ray nanotomography. *Electrochim Acta* 2017;253:85–92. https://doi.org/10.1016/j.electacta.2017.08.161.
- [41] Yufit V, Shearing P, Hamilton RW, Lee PD, Wu M, Brandon NP. Investigation of lithium-ion polymer battery cell failure using X-ray computed tomography. Electrochem Commun 2011;13:608-10. https://doi.org/10.1016/j.elecom. 2011.03.022.
- [42] Kashkooli AG, Foreman E, Farhad S, Lee DU, Feng K, Lui G, et al. Morphological and electrochemical characterization of nanostructured Li4Ti5O12 electrodes using multiple imaging mode synchrotron X-ray computed tomography. J Electrochem Soc 2017;164:A2861–71. doi:10.1149/2.0101713jes.
- [43] Lukas Z, Tobias H, Dean RW, Chien-Wei C, Ingo M, André H, et al. Three-phase multiscale modeling of a LiCoO2 cathode: combining the advantages of FIB-SEM imaging and X-Ray tomography. Adv Energy Mater 2015;5:1401612. doi:10.1002/aenm.201401612.
- [44] Nelson GJ, Ausderau LJ, Shin S, Buckley JR, Mistry A, Mukherjee PP, et al. Transport-geometry interactions in Li-lon cathode materials imaged using X-ray nanotomography. J Electrochem Soc 2017;164:A1412-24. doi:10.1149/2. 0261707jes.
- [45] Withers PJ. X-ray nanotomography. Mater Today 2007;10:26–34. https://doi. org/10.1016/S1369-7021(07)70305-X.
- [46] Pietsch P, Wood V. X-ray tomography for lithium ion battery research: a practical guide. Annu Rev Mater Res 2017;47:451-79. doi:10.1146/ annurev-matsci-070616-123957.
- [47] Martin E, Felix G, Federica M, Marco S, Vanessa W. X-ray tomography of porous, transition metal oxide based lithium ion battery electrodes. Adv Energy Mater 2013;3:845–50. doi:10.1002/aenm.201200932.
- [48] Vierrath S, Zielke L, Moroni R, Mondon A, Wheeler DR, Zengerle R, et al. Morphology of nanoporous carbon-binder domains in Li-ion batteries—A FIB-SEM study. *Electrochem Commun* 2015;60:176–9. https://doi.org/10.1016/j.elecom. 2015.09.010.
- [49] Ender M, Joos J, Carraro T, Ivers-Tiffée E. Quantitative characterization of LiFePO4 cathodes reconstructed by FIB/SEM tomography. J Electrochem Soc 2012;159:A972-80. doi:10.1149/2.033207jes.
- [50] Holzer L, Cantoni M. Review of FIB-tomography. Nanofabrication Using Focused Ion and Electron Beams: Principles and Applications, 559201222 2012:410–35.
- [51] Hutzenlaub T, Asthana A, Becker J, Wheeler DR, Zengerle R, Thiele S. FIB/SEM-based calculation of tortuosity in a porous LiCoO2 cathode for a Li-ion battery. Electrochem Commun 2013;27:77–80. https://doi.org/10.1016/j.elecom. 2012.11.006.
- [52] Joos J, Carraro T, Weber A, Ivers-Tiffée E. Reconstruction of porous electrodes by FIB/SEM for detailed microstructure modeling. J Power Sources 2011;196:7302-7. https://doi.org/10.1016/j.jpowsour.2010.10.006.
- [53] Stephenson DE, Walker BC, Skelton CB, Gorzkowski EP, Rowenhorst DJ, Wheeler DR. Modeling 3D microstructure and ion transport in porous Li-Ion battery electrodes. J Electrochem Soc 2011;158:A781-9. doi:10.1149/1.3579996.
- [54] Mukherjee PP, Kang Q, Wang C-Y. Pore-scale modeling of two-phase transport in polymer electrolyte fuel cells-progress and perspective. *Energy Environ Sci* 2011;4:346-69. doi:10.1039/B926077C.
- [55] Yi Y-B, Wang C-W, Sastry AM. Compression of packed particulate systems: simulations and experiments in graphitic Li-ion anodes. J Eng Mater Technol 2005:128:73–80.
- [56] Gupta A, Jeong Hun S, Xiangchun Z, Wenbo D, Sastry AM, Wei S. Effective transport properties of LiMn2O4 electrode via particle-scale modeling. J Electrochem Soc 2011;158:487–97. doi:10.1149/1.3560441.

- [57] Wang C-W, Sastry AM. Mesoscale modeling of a Li-lon polymer cell. J Electrochem Soc 2007:154:A1035-47. doi:10.1149/1.2778285.
- [58] Wang C-W, Yi Y-B, Sastry AM, Shim J, Striebel KA. Particle compression and conductivity in Li-Ion anodes with graphite additives. J Electrochem Soc 2004:151:A1489-98. doi:10.1149/j.1783909
- [59] Yi Y-B, Wang C-W, Sastry AM. Two-dimensional vs. three-dimensional clustering and percolation in fields of overlapping ellipsoids. J Electrochem Soc 2004;151:A1292–300. doi:10.1149/1.1769272.
- [60] Forouzan MM, Chao C-W, Bustamante D, Mazzeo BA, Wheeler DR. Experiment and simulation of the fabrication process of lithium-ion battery cathodes for determining microstructure and mechanical properties. J Power Sources 2016;312:172–83. https://doi.org/10.1016/j.jpowsour.2016.02.014.
- [61] Wu W, Jiang F. Simulated annealing reconstruction and characterization of the three-dimensional microstructure of a LiCoO2 Lithium-ion battery cathode. *Mater Charact* 2013;80:62–8. https://doi.org/10.1016/j.matchar.2013.03. 011
- [62] Kirkpatrick S. Optimization by simulated annealing: quantitative studies. J Stat Phys 1984;34:975–86. doi:10.1007/BF01009452.
- [63] Siddique N, Salehi A, Liu F. Stochastic reconstruction and electrical transport studies of porous cathode of Li-ion batteries. J Power Sources 2012;217:437– 43. https://doi.org/10.1016/j.jpowsour.2012.05.121.
- [64] Siddique NA, Liu F. Process based reconstruction and simulation of a three-dimensional fuel cell catalyst layer. Electrochim Acta 2010;55:5357-66.
- [65] Mistry AN, Smith K, Mukherjee PP. Secondary-phase stochastics in lithiumion battery electrodes. ACS Appl Mater Interfaces 2018;10:6317–26. doi:10. 1021/acsami.7b17771.
- [66] Mukherjee PP, Wang C-Y, Kang Q. Mesoscopic modeling of two-phase behavior and flooding phenomena in polymer electrolyte fuel cells. *Electrochim Acta* 2009;54:6861–75. https://doi.org/10.1016/j.electacta.2009.06.066.
- [67] Schulz VP, Becker J, Wiegmann A, Mukherjee PP, Wang C-Y. Modeling of two-phase behavior in the gas diffusion medium of PEFCs via full morphology approach. J Electrochem Soc 2007;154:B419–26.
- [68] Wiegmann A. GEODICT: virtual microstructure simulator and material property predictor n.d. https://www.geodict.com/ (accessed June 3, 2018).
- [69] Monaghan JJ. Smoothed particle hydrodynamics. Reports Prog Phys 2005;68:1703-59.
- [70] Tartakovsky AM, Meakin P, Scheibe TD, West RME. Simulations of reactive transport and precipitation with smoothed particle hydrodynamics. J Comput Phys 2007;222:654–72.
- [71] Monaghan JJ. Smoothed particle hydrodynamics and its diverse applications. Annu Rev Fluid Mech 2011;44:323-46. doi:10.1146/ annurev-fluid-120710-101220.
- [72] Lucy LB. A numerical approach to the testing of the fission hypothesis [close binary star formation]. *Astron J* 1977;**82**:1013–24.
- [73] Monaghan JJ, Gingold RA. Smoothed particle hydrodynamics: theory and application to non-spherical stars. *Mon Not R Astron Soc* 1977;**181**:375–89.
- [74] Monaghan JJ, Huppert HE, Worster MG. Solidification using smoothed particle hydrodynamics. J Comput Phys 2005;206:684–705.
- [75] Monaghan JJ, Thompson MC, Hourigan K. Simulation of free surface flows with SPH, vol. 196. Lake Tahoe, NV, USA: Publ by ASME; 1994. p. 375–80.
- [76] Morris JP, Fox PJ, Yi Z. Modeling low Reynolds number incompressible flows using SPH. J Comput Phys 1997;136:214–26.
- [77] Tartakovsky AM, Meakin P. Simulation of unsaturated flow in complex fractures using smoothed particle hydrodynamics. Vadose Zo J 2005;4:848-55.
- [78] Jorn R, Voth GA. Mesoscale simulation of proton transport in proton exchange membranes. J Phys Chem C 2012;116:10476–89. doi:10.1021/jp300040w.
- [79] Zeng J, Wu W, Jiang F. Smoothed particle hydrodynamics prediction of effective transport coefficients of lithium-ion battery electrodes. Solid state ionics. Diffus React 2014;260:76–85. doi:10.1016/j.ssi.2014.03.016.
- [80] Ryan EM, Tartakovsky AM, Recknagle KP, Khaleel MA, Amon CH. Pore scale modeling of the reactive transport of chromium in the cathode of a solid oxide fuel cell. J Power Sources 2011;196:287–300. doi:10.1016/j.jpowsour.2010. 06.030
- [81] Tan J, Tartakovsky AM, Ferris K, Ryan EM. Investigating the effects of anisotropic mass transport on dendrite growth in high energy density lithium batteries. J Electrochem Soc 2016;163:A318–27. doi:10.1149/2.0951602jes.
- [82] Li N, Wei W, Xie K, Tan J, Zhang L, Luo X, et al. Suppressing dendritic lithium formation using porous media in lithium metal-based batteries. *Nano Lett* 2018;18:2067–73. doi:10.1021/acs.nanolett.8b00183.
- [83] Hoogerbrugge P.J., Koelman J.M.V.A. Simulating microscopic hydrodynamic phenomena with dissipative particle dynamics. Eur Lett n.d. 1992;19:155–60.
- [84] Español P, Warren P. Statistical mechanics of dissipative particle dynamics. EPL (Europhysics Lett 1995;30:191.
- [85] Wu D, Paddison SJ, Elliott JA. A comparative study of the hydrated morphologies of perfluorosulfonic acid fuel cell membranes with mesoscopic simulations. Energy Environ Sci 2008;1:284–93. doi:10.1039/b809600g.
- [86] Espanol P, Warren PB. Perspective: dissipative particle dynamics. J Chem Phys 2017;146:150901 (16 pp.)-.
- [87] Xiao Y, Yuan J, Sunden B. Modeling of micro/meso-scale reactive transport phenomena in catalyst layers of proton exchange membrane fuel cells. Int J Low-Carbon Technol 2012;7:280-7. doi:10.1093/ijlct/cts046.
- [88] Chen S, Doolen GD. Lattice Boltzmann method for fluid flows. Annu Rev Fluid Mech 1998;30:329-64. doi:10.1146/annurev.fluid.30.1.329.
- [89] Gunstensen AK, Rothman DH, Zaleski S, Zanetti G. Lattice Boltzmann model of immiscible fluids. Phys Rev A 1991;43:4320–7. doi:10.1103/PhysRevA.43.4320.
- [90] Shan X, Chen H. Lattice Boltzmann model for simulating flows with multiple

- phases and components. *Phys Rev E* 1993;**47**:1815–19. doi:10.1103/PhysRevE. 47.1815.
- [91] Shan X, Chen H. Simulation of nonideal gases and liquid-gas phase transitions by the lattice Boltzmann equation. Phys Rev E 1994;49:2941-8. doi:10.1103/ PhysRevF 40.2941
- [92] Swift MR, Orlandini E, Osborn WR, Yeomans JM. Lattice Boltzmann simulations of liquid-gas and binary fluid systems. *Phys Rev E* 1996;54:5041–52. doi:10.1103/PhysRevE.54.5041.
- [93] Swift MR, Osborn WR, Yeomans JM. Lattice Boltzmann simulation of nonideal fluids. Phys Rev Lett 1995;75:830–3. doi:10.1103/PhysRevLett.75.830.
- [94] He X, Zhang R, Chen S, Doolen GD. On the three-dimensional Rayleigh-Taylor instability. Phys Fluids 1999;11:1143-52. doi:10.1063/1.869984.
- [95] Bhatnagar PL, Gross EP, Krook M. A model for collision processes in gases. I. Small amplitude processes in charged and neutral one-component systems. Phys Rev 1954;94:511–25. doi:10.1103/PhysRev.94.511.
- [96] Mukherjee PP. Pore-scale modeling and analysis of the polymer electrolyte fuel cell catalyst layer. Penn State University; 2007.
- [97] Kang Q, Zhang D, Chen S. Displacement of a two-dimensional immiscible droplet in a channel. *Phys Fluids* 2002;14:3203–14. doi:10.1063/1.1499125.
- [98] Shan X, Doolen G. Diffusion in a multicomponent lattice Boltzmann equation model. Phys Rev E 1996;54:3614–20. doi:10.1103/PhysRevE.54.3614.
- [99] Hou S, Shan X, Zou Q, Doolen GD, Soll WE. Evaluation of two lattice Boltz-mann models for multiphase flows. J Comput Phys 1997;138:695–713. https://doi.org/10.1006/jcph.1997.5839.
- [100] Yang Z.L., Dinh T.N., Nourgaliev R.R., Sehgal B.R. Numerical investigation of bubble growth and detachment by the lattice-Boltzmann method. Int J Heat Mass Transf n.d. 2001;44:195–206.
- [101] Dorenbos G. Pore network design: DPD-Monte Carlo study of solvent diffusion dependence on side chain location. J Power Sources 2014;270:536–46. doi:10.1016/j.jpowsour.2014.07.156.
- [102] Lee SG, Jeon DH, Kim BM, Kang JH, Kim C-J. Lattice Boltzmann simulation for electrolyte transport in porous electrode of lithium ion batteries. J Electrochem Soc 2013;160:H258-65. doi:10.1149/2.017306jes.
- [103] Tabe Y, Lee Y, Chikahisa T, Kozakai M. Numerical simulation of liquid water and gas flow in a channel and a simplified gas diffusion layer model of polymer electrolyte membrane fuel cells using the lattice Boltzmann method. J Power Sources 2009;193:24–31. doi:10.1016/j.jpowsour.2009.01.068.
- [104] Ben Amara MEA, Ben Nasrallah S. Numerical simulation of droplet dynamics in a proton exchange membrane (PEMFC) fuel cell micro-channel. Int J Hydrogen Energy 2015;40:1333–42. doi:10.1016/j.ijhydene.2014.09.077.
- [105] Wu D, Paddison SJ, Elliott JA, Hamrock SJ. Mesoscale modeling of hydrated morphologies of 3m perfluorosulfonic acid-based fuel cell electrolytes. *Lang-muir* 2010;26:14308–15. doi:10.1021/la102358y.
- [106] Chen L, He Y, Tao W-Q, Zelenay P, Mukundan R, Kang Q. Pore-scale study of multiphase reactive transport in fibrous electrodes of vanadium redox flow batteries. *Electrochim Acta* 2017;248:425–39. doi:10.1016/j.electacta.2017. 07.086
- [107] Qiu G, Joshi AS, Dennison CR, Knehr KW, Kumbur EC, Sun Y. 3-D pore-scale resolved model for coupled species/charge/fluid transport in a vanadium redox flow battery. *Electrochim Acta* 2012;64:46–64. doi:10.1016/j.electacta.2011. 12.065
- [108] Mohammadian SK, Zhang Y. Improving wettability and preventing Li-ion batteries from thermal runaway using microchannels. Int J Heat Mass Transf 2018;118:911–18. doi:10.1016/j.ijheatmasstransfer.2017.11.063.
- [109] He S, Habte BT, Jiang F. LBM prediction of effective electric and species transport properties of lithium-ion battery graphite anode. Solid State Ionics, Diffus React 2016;296:146-53. doi:10.1016/j.ssi.2016.09.021.
- [110] Jiang ZY, Qu ZG, Zhou L, Tao WQ. A microscopic investigation of ion and electron transport in lithium-ion battery porous electrodes using the lattice Boltzmann method. *Appl Energy* 2017;194:530–9. doi:10.1016/j.apenergy.2016. 10.125
- [111] He S, Habte BT, Jiang F. LBM prediction of effective thermal conductivity of lithium-ion battery graphite anode. Int Commun Heat Mass Transf 2017;82:1– 8. doi:10.1016/j.icheatmasstransfer.2017.02.015.
- [112] Tan J, Ryan EM. Structured electrolytes to suppress dendrite growth in high energy density batteries. *Int J Energy Res* 2016;**40**:1800–10. doi:10.1002/er. 3560.
- [113] Espinoza M, Sunden B, Andersson M, Yuan J. Analysis of porosity and tortuosity in a 2D selected region of solid oxide fuel cell cathode using the lattice Boltzmann method. ECS Trans 2015;65:59–73. doi:10.1149/06501.0059ecst.
- [114] Paradis H, Andersson M, Sunden B. Modeling of mass and charge transport in a solid oxide fuel cell anode structure by a 3D lattice Boltzmann approach. Heat Mass Transf Und Stoffuebertragung 2016;52:1529-40. doi:10.1007/ s00231-015-1670-8.
- [115] Shimura T, Jiao Z, Shikazono N. Evaluation of nickel-yttria stabilized zirconia anode degradation during discharge operation and redox cycles operation by electrochemical calculation. J Power Sources 2016;330:149–55. doi:10.1016/j. jpowsour.2016.09.006.
- [116] He A, Kim Y, Shikazono N. Three-dimensional numerical simulation of solid oxide fuel cell cathode based on lattice Boltzmann method with subgrid scale models. Int J Hydrogen Energy 2017;42:21886–900. doi:10.1016/j. iihydene.2017.07.074.
- [117] Dang Z, Xu H. Pore scale investigation of gaseous mixture flow in porous anode of solid oxide fuel cell. *Energy* 2016;107:295–304. doi:10.1016/j.energy. 2016.04.015.
- [118] Yang C, He H, Zhou N, Peng W, Yang K. Telescopic projective Adams multi-

- scale modeling of electrochemical reactions in tubular solid oxide fuel cells. *Comput Chem Eng* 2016;**93**:331–42. doi:10.1016/j.compchemeng.2016.07.016.
- [119] Ryan EM, Xu W, Sun X, Khaleel MA. A damage model for degradation in the electrodes of solid oxide fuel cells: modeling the effects of sulfur and antimony in the anode. J Power Sources 2012;210:233–42. doi:10.1016/j.jpowsour. 2012.02.091.
- [120] Joshi AS, Peracchio AA, Grew KN, Chiu WKS. Lattice Boltzmann method for continuum, multi-component mass diffusion in complex 2D geometries. J Phys D Appl Phys 2007;40:2961–71.
- [121] Grew KN, Chiu WKS. A review of modeling and simulation techniques across the length scales for the solid oxide fuel cell. J Power Sources 2012;199:1–13. doi:10.1016/i.ipowsour.2011.10.010.
- [122] Tan J, Ryan EM. Computational study of electro-convection effects on dendrite growth in batteries. J Power Sources 2016;323:67–77. doi:10.1016/j.jpowsour. 2016.05.012.
- [123] Andrea A, Giordano A, Roberto G. A 3D fully Lagrangian smoothed particle hydrodynamics model with both volume and surface discrete elements. Int J Numer Methods Eng 2013;95:419–50. doi:10.1002/nme.4514.
- [124] Monaghan JJ, Kajtar JB. SPH particle boundary forces for arbitrary boundaries. Comput Phys Commun 2009;180:1811–20. https://doi.org/10.1016/j.cpc. 2009.05.008.
- [125] Colagrossi A, Landrini M. Numerical simulation of interfacial flows by smoothed particle hydrodynamics. J Comput Phys 2003;191:448–75. https: //doi.org/10.1016/S0021-9991(03)00324-3.
- [126] Colagrossi A, Antuono M, Souto-Iglesias A, Le Touzé D. Theoretical analysis and numerical verification of the consistency of viscous smoothed-particlehydrodynamics formulations in simulating free-surface flows. *Phys Rev E* 2011;84:26705. doi:10.1103/PhysRevE.84.026705.
- [127] Mistry A, Juarez-Robles D, Stein M, Smith K, Mukherjee PP. Analysis of longrange interaction in lithium-ion battery electrodes. J Electrochem Energy Convers Storage 2016;13(3) 031006–(1–13). doi:10.1115/1.4035198.
- [128] Chen C-F, Verma A, Mukherjee PP. Probing the role of electrode microstructure in the lithium-ion battery thermal behavior. J Electrochem Soc 2017;164:E3146–58. doi:10.1149/2.0161711jes.
- [129] Wiedemann AH, Goldin GM, Barnett SA, Zhu H, Kee RJ. Effects of three-dimensional cathode microstructure on the performance of lithium-ion battery cathodes. *Electrochim Acta* 2013;88:580–8. doi:10.1016/j.electacta.2012.10.
- [130] Smith M, Garcia RE, Horn QC. The effect of microstructure on the galvanostatic discharge of graphite anode electrodes in LiCoO2-based rocking-chair rechargeable batteries. J Electrochem Soc 2009;156:A896-904. doi:10.1149/1. 3216000.
- [131] García E, Chiang YM, Carter W, Limthongkul P, Bishop CM. Microstructural modeling and design of rechargeable lithium-ion batteries 2005;**152**:A255–63. doi:10.1149/1.1836132.
- [132] Garcia RE, Yet-Ming C. Spatially resolved modeling of microstructurally complex battery architectures. J Electrochem Soc 2007;154:A856–64. doi:10.1149/1.2754072.
- [133] Malavé V, Berger JR, Zhu H, Kee RJ. A Computational model of the mechanical behavior within reconstructed LixCoO2 Li-ion battery cathode particles. *Electrochim Acta* 2014;130:707–17. https://doi.org/10.1016/j.electacta.2014.03.113.
- [134] Goldin GM, Colclasure AM, Wiedemann AH, Kee RJ. Three-dimensional particle-resolved models of Li-ion batteries to assist the evaluation of empirical parameters in one-dimensional models. *Electrochim Acta* 2012;**64**:118–29. https://doi.org/10.1016/j.electacta.2011.12.119.
- [135] Zienkiewicz O, Taylo R. The finite element method. 7th ed. Butterworth-Heinemann; 2013.
- [136] Eymard R, Gallouët T. Herbin RBT-H of NA. Finite volume methods. Solut. Equ.  $\mathbb{R}$  (Part 3), Tech. Sci. Comput. (Part 3), vol. 7. Elsevier; 2000. p. 713–1018.
- [137] Kotaka T, Tabuchi Y, Mukherjee PP. Microstructural analysis of mass transport phenomena in gas diffusion media for high current density operation in PEM fuel cells. J Power Sources 2015;280:231–9. https://doi.org/10.1016/j.jpowsour. 2015.01.111
- [138] Newman J, Tiedemann W. Porous-electrode theory with battery applications. AIChE J 1975;21:25–41. doi:10.1002/aic.690210103.
- [139] Doyle M, Fuller TF, Newman J. Modeling of galvanostatic charge and discharge of the lithium/polymer/insertion cell. *J Electrochem Soc* 1993;**140**:1526–33. doi:10.1149/1.2221597
- [140] Ebner M, Chung D-W, García RE, Wood V. Tortuosity anisotropy in lithiumion battery electrodes. Adv Energy Mater 2013;4:1301278. doi:10.1002/aenm. 201301278
- [141] Kehrwald D, Shearing PR, Brandon NP, Sinha PK, Harris SJ. Local tortuosity inhomogeneities in a lithium battery composite electrode. J Electrochem Soc 2011;158:A1393–9. doi:10.1149/2.079112jes.

- [142] Trembacki BL, Mistry AN, Noble DR, Ferraro ME, Mukherjee PP, Roberts SA. Editors' choice—mesoscale analysis of conductive binder domain morphology in lithium-ion battery electrodes. J Electrochem Soc 2018;165:E725–36. doi:10. 1149/2.0981813jes.
- [143] Usseglio-Viretta FLE, Colclasure A, Mistry AN, Claver KPY, Pouraghajan F, Finegan DP, et al. Resolving the discrepancy in tortuosity factor estimation for liion battery electrodes through micro-macro modeling and experiment. *J Electrochem Soc* 2018;**165**:A3403–26. doi:10.1149/2.0731814jes.
- [144] Mistry AN, Smith K, Mukherjee PP. Electrochemistry coupled mesoscale complexations in electrodes lead to thermo-electrochemical extremes. ACS Appl Mater Interfaces 2018:10:28644-55.
- [145] Mistry AN, Mukherjee PP. Precipitation–microstructure interactions in the lisulfur battery electrode. *J Phys Chem C* 2017;121:26256–64.
- [146] Chen C-F, Mistry A, Mukherjee PP. Probing impedance and microstructure evolution in lithium-sulfur battery electrodes. J Phys Chem C 2017;121:21206– 16. doi:10.1021/acs.jpcc.7b07245.
- [147] Mistry AN, Mukherjee PP. Probing spatial coupling of resistive modes in porous intercalation electrodes through impedance spectroscopy. *Phys Chem Chem Phys* 2018. doi:10.1039/C8CP05109G.
- [148] Zhao K, Wang WL, Gregoire J, Pharr M, Suo Z, Vlassak JJ, et al. Lithium-assisted plastic deformation of silicon electrodes in lithium-ion batteries: a first-principles theoretical study. *Nano Lett* 2011;**11**:2962–7. doi:10.1021/nl201501s.
- [149] Barai P, Huang B, Dillon SJ, Mukherjee PP. Mechano-electrochemical interaction gives rise to strain relaxation in Sn electrodes. J Electrochem Soc 2016;163:A3022-35. doi:10.1149/2.0801614jes.
- [150] Wood KN, Kazyak E, Chadwick AF, Chen K-H, Zhang J-G, Thornton K, et al. Dendrites and pits: untangling the complex behavior of lithium metal anodes through operando video microscopy. ACS Cent Sci 2016;2:790–801. doi:10. 1021/acscentsci.6b00260.
- [151] Wang T, Villegas Salvatierra R, Jalilov AS, Tian J, Tour JM. Ultrafast charging high capacity asphalt-lithium metal batteries. ACS Nano 2017;11:10761-7. doi:10.1021/acsnano.7b05874.
- [152] Mukherjee PP, Wang CY. Stochastic microstructure reconstruction and direct numerical simulation of the PEFC catalyst layer. J Electrochem Soc 2006;153:A840–9.
- [153] Mukherjee PP, Wang CY. Direct numerical simulation modeling of bilayer cathode catalyst layers in polymer electrolyte fuel cells. J Electrochem Soc 2007;154:B1121-31.
- [154] Kim SH, Pitsch H. Reconstruction and effective transport properties of the catalyst layer in pem fuel cells. J Electrochem Soc 2009;156:B673–81. doi:10.1149/ 1.3106136.
- [155] Inoue G, Kawase M. Effect of porous structure of catalyst layer on effective oxygen diffusion coefficient in polymer electrolyte fuel cell. J Power Sources 2016;327:1–10. doi:10.1016/j.jpowsour.2016.07.037.
- [156] Komini Babu S, Chung HT, Zelenay P, Litster S. Resolving electrode morphology's impact on platinum group metal-free cathode performance using nano-CT of 3D hierarchical pore and ionomer distribution. ACS Appl Mater Interfaces 2016;8:32764–77. doi:10.1021/acsami.6b08844.
- [157] Zheng W, Kim SH. A multiscale approach to accelerate pore-scale simulation of porous electrodes. J Power Sources 2017;348:21–9. doi:10.1016/j.jpowsour. 2017.02.073
- [158] Yan B, Lim C, Yin L, Zhu L. Three dimensional simulation of galvanostatic discharge of LiCoO2 cathode based on X-ray nano-CT images. J Electrochem Soc 2012;159:A1604–14. doi:10.1149/2.024210jes.
- [159] Trembacki BL, Noble DR, Brunini VE, Ferraro ME, Roberts SA. Mesoscale effective property simulations incorporating conductive binder. J Electrochem Soc 2017;164:E3613–26. doi:10.1149/2.0601711jes.
- [160] Zahn R, Lagadec MF, Wood V. Transport in lithium ion batteries: reconciling impedance and structural analysis. ACS Energy Lett 2017;2:2452–3. doi:10.1021/acsenergylett.7b00740.
- [161] Holdren JP. Materials genome initiative for global competitiveness. General Books; 2011.
- [162] Effat M.B., Wu C., Ciucci F. Modeling efforts in the key areas of thermal management and safety of lithium ion battery cells: a mini review. Asia-Pac J Chem Eng n.d. 2016;11:399–406.
- [163] Abada S, Marlair G, Lecocq A, Petit M, Sauvant-Moynot V, Huet F. Safety focused modeling of lithium-ion batteries: a review. J Power Sources 2016;306:178-92. https://doi.org/10.1016/j.jpowsour.2015.11.100.
- [164] Liu B, Yin S, Xu J. Integrated computation model of lithium-ion battery subject to nail penetration. *Appl Energy* 2016;183:278–89. https://doi.org/10.1016/j.apenergy.2016.08.101.